EES Solar

REVIEW

View Article Online
View Journal

Check for updates

Cite this: DOI: 10.1039/d6el00030d

Probing surfaces and interfaces of halide perovskites: from atomic mapping to optoelectronic properties

Zhang Qu, Jing Chen, Bin Xue and Shuang Xiao *

Halide perovskites have exhibited outstanding optoelectronic properties and been widely applied in the fields of solar cells, detectors, and light emitting diodes. Surfaces and interfaces are crucial for the performance of the perovskite-based devices, as they could significantly influence carrier transport, recombination and so forth. This review covers the state-of-the-art techniques for characterizing the surface and interface of halide perovskites, focusing on scanning probe microscopy (SPM) and complementary techniques for high-resolution characterization. It explores conventional SPM methods, such as scanning tunneling microscopy (STM), atomic force microscopy (AFM), Kelvin probe force microscopy (KPFM) and their applications in topography and optoelectronic properties. The discussion extends to integrated SPM-based optoelectronic detection technologies like scanning near-field optical microscopy (SNOM), photoluminescence-AFM (PL-AFM), AFM-infrared spectroscopy (AFM-IR), and surface photovoltage microscopy (SPVM). Additionally, the review encompasses time-resolved methodologies, including time-resolved KPFM (tr-KPFM) and pump-probe KPFM (pp-KPFM), which are highlighted for their role in capturing ultrafast dynamic processes. Collectively, these tools provide a complete structural and optoelectronic analysis, significantly enhancing our understanding of the surfaces and interfaces of perovskites and driving advancements in materials science and technology.

Received 15th February 2026
Accepted 24th March 2026

DOI: 10.1039/d6el00030d

rsc.li/EESSolar

Open Access Article. Published on 26 March 2026. Downloaded on 6/16/2026 7:27:17 AM.
This article is licensed under a Creative Commons Attribution-NonCommercial 3.0 Unported Licence.

Broader context

Understanding surfaces and interfaces in halide perovskites is essential because their optoelectronic properties are highly sensitive to grain boundaries, vacancies, and interstitial defects, all of which strongly affect device efficiency and stability. While conventional macroscopic techniques provide valuable information on overall device behavior, they generally lack the spatial and temporal resolution required to resolve nanoscale heterogeneities and dynamic interfacial processes. In this review, we present an overview of recent advances in the high-resolution characterization of perovskite surfaces and interfaces, with a focus on SPM and its derivative techniques. We summarize the principles and applications of AFM, STM, and KPFM for atomic-scale structural and electronic mapping, and discuss how integrating SPM with optical and spectroscopic approaches enables direct probing of local optoelectronic phenomena. Emerging techniques, including SNOM, PL-AFM, AFM-IR, SPVM, as well as time-resolved methods such as tr-KPFM and pump-probe KPFM, are highlighted for their ability to capture transient carrier dynamics with high spatiotemporal resolution.

1 Introduction

The rapid technological advancement and industrial growth cause an accelerating global energy demand and environmental degradation, which underscore the urgent need for clean and sustainable energy sources. Among various renewable energy resources, solar energy stands out as one of the most abundant, direct, and environmentally friendly options. Until now, solar cells have been applied in many respects in our daily life. However, the efficiency of solar cells that are currently harvested and utilized remains suboptimal, largely constrained by limitations in material properties and architecture. Perovskite solar cells (PSCs) have emerged as a promising option, revolutionizing the field of photovoltaics with their exceptional optoelectronic properties.[1–7] Halide perovskites typically have the general formula ABX_3 (where A = Cs^+, MA^+, FA^+; B = Pb^{2+}, Sn^{2+}; X = I^-, Br^- and Cl^-); the distinctive crystal structure endows them with exceptional optoelectronic conversion efficiency, which has enabled their widespread application in the photovoltaic industry and in radiation detection technologies.[8–16] Their favorable attributes, including tunable bandgaps, strong light absorption, long carrier diffusion lengths, and compatibility with low-temperature solution processing, position PSCs as strong contenders to conventional silicon-based solar technologies.[17–22] Excitingly, PSCs have demonstrated fast and unprecedented improvements in power conversion efficiency (PCE), now exceeding 27.0%.[23–30]

Shenzhen Key Laboratory of Ultraintense Laser and Advanced Material Technology, Center for Intense Laser Application Technology, College of Engineering Physics, Shenzhen Technology University, Shenzhen 518118, China. E-mail: xiaoshuang@sztu.edu.cn

© 2026 The Author(s). Published by the Royal Society of Chemistry

Open Access Article. Published on 26 March 2026. Downloaded on 6/16/2026 7:27:17 AM. This article is licensed under a Creative Commons Attribution-NonCommercial 3.0 Unported Licence.

Despite these advancements, several challenges impede the commercialization of PSCs. Notably, issues related to operational stability, scalability, lead toxicity, and device reproducibility remain unresolved.[31–36] A central origin of these challenges lies in the complex and dynamic behavior of surfaces and interfaces within perovskite-based devices.[37–43] Surface and interface studies have been fundamental in the development of semiconductor technologies, and they continue to be of paramount importance in the optimization of next-generation optoelectronic and photovoltaic devices. Structural imperfections such as grain boundaries (GBs), vacancies, and interstitial defects, especially at surfaces and interfaces, act as non-radiative recombination centers, limiting charge carrier lifetimes and device efficiency.[44–48] Inhomogeneities at the atomic scale can further exacerbate these effects, leading to current density–voltage (*J–V*) hysteresis, ion migration, and performance degradation over time. The interfaces between the perovskite, electron transport layer (ETL), and hole transport layer (HTL) play a critical role in determining energy level alignment, carrier extraction efficiency, and overall device stability. In addition, ion migration can induce interfacial degradation, phase segregation, and internal electric field screening, all of which undermine long-term performance.[49]

To fundamentally elucidate the structure property relationships that dictate the performance of PSCs, it is crucial to employ advanced characterization techniques with both high spatial and temporal resolution, particularly at their structurally and chemically complex surfaces and interfaces.[50] Conventional methods such as scanning electron microscopy (SEM) and transmission electron microscopy (TEM) are widely used to investigate the morphology, bulk composition, and crystallinity of the perovskite layer. Techniques like X-ray diffraction (XRD), X-ray photoelectron spectroscopy (XPS), and photoluminescence (PL) spectroscopy provide insight into the crystal structure, chemical states, optical properties, and energy-level alignment of the materials.[22,51–54] Electrical characterization methods, including *J–V* measurements, capacitance–voltage (*C–V*) profiling, and transient response analyses, are commonly used to assess key device parameters such as defects, mobility, and charge carrier lifetime.[55–57] While these macroscopic techniques offer valuable information on overall device behavior, they generally lack the spatial resolution necessary to resolve nanoscale heterogeneities or atomic-scale defects that can critically impact performance. Furthermore, many of these methods involve high-energy radiation or intense illumination, which can cause irreversible damage to the perovskite material, thus limiting their suitability for *in situ* or repeatable measurements.

Scanning probe microscopy (SPM) has emerged as a critical tool for surface and interface characterization of halide perovskites.[58–64] Since the invention of scanning tunneling microscopy (STM) in 1981 and atomic force microscopy (AFM) in 1986, SPM techniques have become indispensable for nanoscience.[61,65,66] STM enables direct imaging of electronic structures on conductive surfaces with atomic resolution,[67–72] whereas AFM broadens the applicability to insulating and soft materials, including halide perovskites, based on tip–sample interaction forces.[48,73–98] Notably, AFM-derived techniques offer multifaceted capabilities that extend beyond topographic mapping. In Fig. 1, we outline the related SPM technologies for measuring halide perovskites. For example, conductive AFM (c-AFM) can spatially correlate morphology with local conductivity, identifying features in charge transport at the nanoscale.[54,62,99–107] Kelvin probe force microscopy (KPFM) enables quantitative surface potential measurements, allowing researchers to visualize charge redistribution, band bending, and ion migration at GBs and heterointerfaces,[60,104,108–121] which is widely used in the perovskite community.[122–133] These phenomena are directly linked to performance issues such as charge behavior, and device instability. More advanced KPFM-based methods, including time-resolved KPFM (tr-KPFM) and pump-probe KPFM (pp-KPFM), allow dynamic tracking of carrier trapping, recombination, and ion migration processes with sub-millisecond to nanosecond temporal resolution.[118,134–149] These techniques provide insights into transient electronic behavior under operating conditions, bridging the gap between static imaging and real device performance.

On the other hand, investigating PSCs inherently requires understanding of how illumination affects material properties. Surface photovoltage (SPV) measurements integrated with AFM tips enable *in situ* probing of optoelectronic responses, such as the efficiency of photogenerated charge separation.[136–138,146] The integration of AFM with optical techniques is not limited to conventional light sources; coupling AFM with advanced laser systems allows for deeper exploration of surface physical phenomena. Recent advancements in hybrid AFM platforms have significantly expanded the analytical capabilities of these techniques. For instance, scanning near-field optical microscopy (SNOM) combines focused laser excitation with AFM tips to achieve localized field enhancement, thereby enabling *in situ* optical measurements with high spatial resolution well beyond the diffraction limit.[150–157] Photoluminescence-AFM (PL-AFM), which simultaneously maps surface topography and local luminescence, reveals critical relationships between structural features and charge recombination behavior.[150,158,159] Likewise, AFM-infrared spectroscopy (AFM-IR) provides nanoscale-resolved chemical composition analysis,[158–161] which is essential for understanding interfacial degradation mechanisms. These multimodal techniques enable nano- to atomic-scale analysis in both spatial and spectroscopic dimensions, surpassing the limitations of traditional optical methods. Moreover, incorporating modulated laser excitation into pump-probe KPFM (pp-KPFM) setups has significantly improved the temporal resolution of KPFM-based measurements, enabling the study of dynamic charge carrier processes and surface potential changes on the picosecond timescale.[135]

In this review, we present a systematic overview of the above state-of-the-art SPM techniques and their integration with optical and time-resolved methodologies for characterizing perovskite materials and devices. These SPM-based approaches facilitate simultaneous nanoscale mapping of morphological, electronic, and optical properties, offering a comprehensive understanding of how local heterogeneities impact

 © 2026 The Author(s). Published by the Royal Society of Chemistry

Open Access Article. Published on 26 March 2026. Downloaded on 6/16/2026 7:27:17 AM.
This article is licensed under a Creative Commons Attribution-NonCommercial 3.0 Unported Licence.

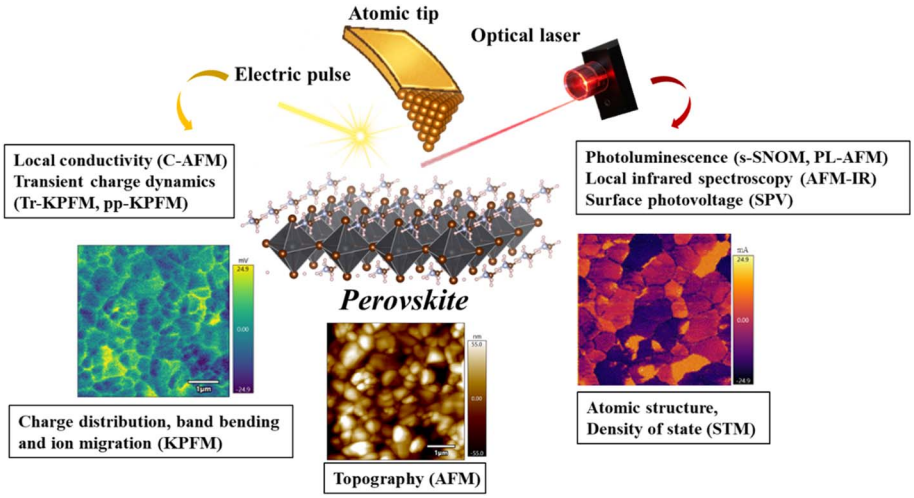

Fig. 1 Schematic illustration of SPM-based techniques applied to halide perovskites. Utilizing an atomic tip, researchers can resolve their surface topography, density of states, and charge distributions with high spatial resolution. When combined with laser excitation or electric pulses, these approaches can further enable the characterization of optical responses and transient electrostatic properties.

macroscopic device performance. These advanced multimodal platforms offer unique opportunities to unravel the fundamental physical and optical processes at surfaces and interfaces, which are key to enhancing the efficiency, stability, and scalability of PSCs.

2 Scanning probe microscopy for halide perovskites

2.1 Atomic-resolution characterization of surface structures

AFM has been extensively employed to characterize surface morphology across a wide range of material systems, including halide perovskites. As schematically illustrated in Fig. 2a, a conventional optical beam deflection AFM (OBD-AFM) system consists of a nanoscale tip mounted on a silicon cantilever, typically with a radius of less than 5 nm. As the tip approaches the sample surface, interaction forces between the tip and sample such as van der Waals forces, electrostatic forces, and short-range chemical interactions, induce deflections of the cantilever.[75] These deflections are detected by monitoring the reflection of a laser beam onto a photodetector and are translated into high-resolution topographic images. When AFM operated at noncontact mode and in the vacuum environment, a surface structure with atomic resolution can be obtained.[75]

In an alternative AFM configuration, a qPlus sensor is employed,[74] in which a quartz tuning fork serves as the oscillation sensor with a metallic tip mounted at the end (Fig. 2b). Compared to OBD-AFM, qPlus-AFM typically operates at higher resonance frequencies and smaller oscillation amplitudes and enables precise detection of frequency shifts induced by short-range interactions, thus facilitating atomic-scale imaging. To further enhance spatial resolution and achieve chemical force imaging at the atomic scale, functionalized tips have been developed. For example, a carbon monoxide (CO) molecule can be absorbed on the tip apex, effectively reducing the tip radius to the size of a single atom.[162–165] Due to the well-defined bond length and weak binding of the CO molecule, even subtle variations in surface forces which arise from interatomic interactions within the target molecules can induce significant shifts in the tip's oscillatory behavior. Observation of chemical contrast and even the resolution of individual intramolecular bonds can be achieved, representing a significant advancement in AFM.

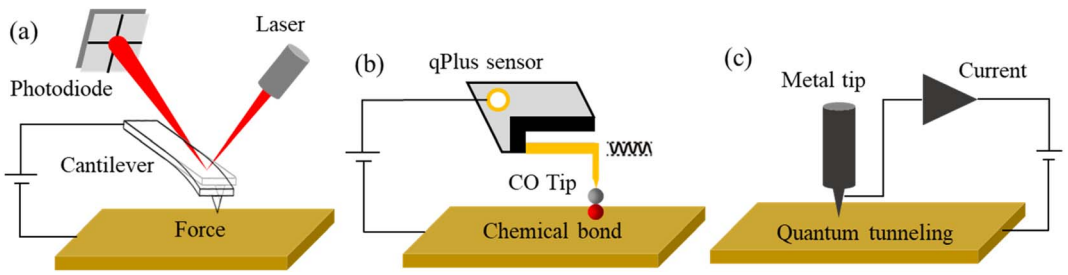

Fig. 2 Schematics of major SPM techniques for imaging halide perovskites. (a) OBD-AFM, tip–sample interaction force is detected using an oscillated cantilever. (b) qPlus-AFM, chemical bonds can be identified using a CO functional tip. (c) STM, quantum tunneling can be measured using a sharp conductive tip through a preamplifier.

Open Access Article. Published on 26 March 2026. Downloaded on 6/16/2026 7:27:17 AM. This article is licensed under a Creative Commons Attribution-NonCommercial 3.0 Unported Licence.

Moreover, another important function of AFM lies in its ability to measure the relationship between the local interaction force and the tip–sample distance, known as force spectroscopy.[56] At different tip–sample separations, various types of interaction forces contribute differently to the total measured force—for example, long-range van der Waals forces, short-range chemical forces, electrostatic forces, and Pauli repulsion. By analyzing force spectra acquired at distinct surface locations, one can effectively identify and differentiate various structural features of the sample surface.

STM provides atomic-resolution imaging by exploiting the quantum tunneling of electrons between a conductive tip and the sample surface under an applied bias voltage, once their separation is reduced to a few ångströms (Fig. 2c).[166,167] As a current-based technique, STM is intrinsically sensitive to the local electronic density of states (LDOS), making it particularly effective for probing surface electronic structures such as band edges, defect states, and charge localization phenomena. However, due to the semiconductor property and moderate conductivity of halide perovskites, STM measurements typically require ultrahigh vacuum (UHV) conditions and cryogenic temperatures to achieve stable tunneling currents, often aided by relatively high bias voltages.[72,168]

Furthermore, high-resolution STM images can be realized utilizing OBD-AFM and qPlus-AFM. In this approach, a metallic tip is employed to generate a tunneling current when it approaches the conductive sample under an applied bias voltage. Distinct from conventional STM, the tunneling current is measured while the tip is in an oscillating state. The high-frequency and small-amplitude oscillation of the AFM sensor is particularly conducive to obtaining high-resolution current mapping. In addition, a preamplifier and a low-pass filter are required to amplify and process the current signal for precise electronic acquisition.

Achieving atomic-scale resolution in UHV-based STM, OBD-AFM, and qPlus-AFM measurements imposes stringent requirements on the structural and electronic quality of perovskite samples. The sample surface must exhibit atomically flat terraces with well-ordered lattice structures extending over tens of nanometers. For bulk perovskite crystals, precise cleaving procedures are typically necessary to expose pristine and well-defined surfaces suitable for AFM characterization. In the case of perovskite thin films, such as those prepared *via* CVD, the film thickness is generally restricted to below ~100 nm to ensure sufficient electrical conductivity for STM measurements. As the tunneling current decays exponentially with tip–sample separation and is intrinsically weak, excessive resistance within the semiconductor layer can significantly attenuate the measurable signal. Therefore, rigorous control over film thickness and the establishment of reliable electrical contact are essential for obtaining stable tunneling currents and high-quality imaging.

The selection of an appropriate substrate and material system is of equal significance. Conductive metallic substrates, including Au, Ag, or Cu, are frequently utilized in UHV experiments to provide both chemical stability and efficient electrical grounding while minimizing substrate-induced perturbations to the electronic properties of the perovskite layer. Furthermore, in the investigation of low-dimensional or heterostructure of perovskites, the molecular composition must be strategically engineered to ensure structural robustness and suppress potential interfacial reactions during measurement. For example, in two-dimensional/three-dimensional (2D/3D) perovskite heterostructures, large organic cations are typically incorporated to stabilize the 2D layers, while smaller cations serve to preserve the structural integrity of the 3D perovskite framework.

2.1.1 Atomic force microscopy with a qPlus sensor (qPlus-AFM). To achieve atomic resolution of perovskite surface, noncontact mode AFM (ncAFM) under UHV and cryogenic conditions are necessary. A notable study is achieved by K. Leng *et al.*; they successfully visualized the surface lattice of Ruddlesden–Popper perovskites (RPPs, $BA_2MA_{n-1}Pb_nI_{3n+1}$) on an Au (111) substrate using ncAFM equipped with a qPlus sensor.[169] Fig. 3a shows the structural model of 2D RPPs. Fig. 3b displays the large-scale topography of the perovskite film grown on the Au (111) substrate. Clear steps and sharp boundaries of the perovskite layer are observed. By analyzing the height profile across the boundary, a thickness of approximately 1.4 nm is determined, which corresponds to a single layer of 2D perovskite layer (Fig. 3a and c). The atomic resolution topography images were obtained at low temperature (78 K), with annealing samples at different temperatures after perovskite layer formation. In Fig. 3d, the image reveals a well-defined square lattice structure without annealing, where the bright features were attributed to surface-bound butylammonium (BA^+) organic cations. Due to the intrinsic contrast limitations, the inner PbI^- framework was not directly resolved, yet structural relaxation phenomena could still be discerned. Upon annealing the sample at 60 °C, the AFM images revealed a transformation into zigzag domain structures (Fig. 3e), attributed to the reorganization of BA^+ chains at the surface. When the sample is annealed up to 90 °C, most of the structures show a zigzag domain (Fig. 3f). Vertical structural variations were further investigated by analyzing height profiles along selected lines in Fig. 3f, with the results shown in Fig. 3g. These profiles demonstrate that ncAFM can achieve sub-ångström vertical resolution, down to a few picometers. Moreover, ncAFM provides direct access to local interaction forces. When tip scanning at a constant height, the tip–sample interaction is revealed by the frequency shift (Δf) of tip oscillation. Therefore, by measuring the Δf as a function of tip–sample distance (z), force spectra can be estimated. Fig. 3h and i are constant height AFM images at $\Delta f = -8$ Hz and $\Delta f = -7.5$ Hz, respectively. In Fig. 3j, force spectra are measured at three points marked in Fig. 3h, and an inversion point is observed at the tip–sample distance between $\Delta f = -8$ Hz and $\Delta f = -7.5$ Hz. Therefore, the spatially dependent contrast inversions are obtained and shown in Fig. 3h and i, highlighting the sensitivity of AFM in vertical tip–sample interactions. Such force-based imaging provides additional insights into the material's local electronic and mechanical properties beyond conventional topography.

Furthermore, when temperature decreases to 4 K, tips can be functionalized with a CO molecule, which dramatically

 © 2026 The Author(s). Published by the Royal Society of Chemistry

Open Access Article. Published on 26 March 2026. Downloaded on 6/16/2026 7:27:17 AM.
This article is licensed under a Creative Commons Attribution-NonCommercial 3.0 Unported Licence.

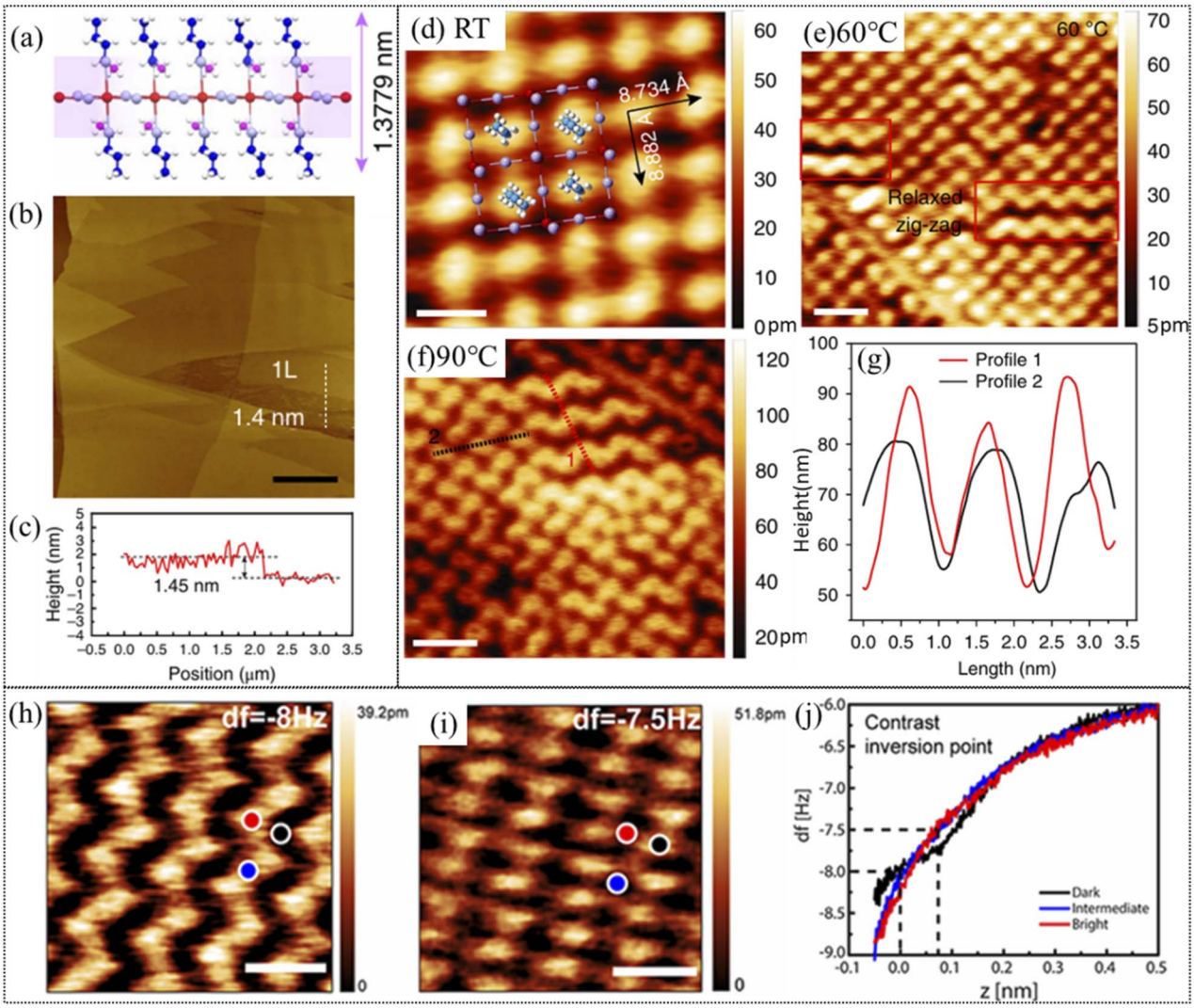

Fig. 3 Atomic-scale characterization of 2D Ruddlesden–Popper perovskites by using qPlus-AFM at low temperature (78 K). (a) Structural model and (b) topographic image of monolayer 2D-RPPs. Scale bars, 4 μm. (c) Height profile along the white line in (b), the height of the step corresponding to the monolayer model well. (d–f) Atomic topographic images of monolayer 2D-RPPs of the annealing sample at RT, 60 °C, and 90 °C. (g) Height profiles of zigzag and square lattices along lines in (f). (h and i) Different topographic contrasts in the same area when imaging at different tip heights. (j) Force spectra at three points in (i). Scale bar 1 nm (d–i). Reproduced from ref. 169 with permission from Springer Nature,[169] copyright 2018.

improves spatial resolution and the chemical sensitivity of imaging. M. Telychko *et al.* has successfully obtained bond-resolution images of the perovskite monolayer using a CO-terminated qPlus-AFM probe (Fig. 4).[170] They revealed critical molecular-level details, including the orientation of organic cations and local surface phase arrangements, offering valuable insights into structure–property relationships in organic–inorganic hybrid perovskites.

The images in Fig. 4a and b were obtained by constant-height mode. The Δf contrast reflects the spatial variation in tip–sample interactions, which mainly arise from short-range Pauli repulsion forces between the CO-functionalized tip and the sample surface. A representative high-resolution image of the RPP surface (Fig. 4a) displays a periodic square lattice of "arrow-like" features.[170] These features correspond to BA^+ cations adsorbed on the surface, with each "arrow" attributed to a pair of apical methyl ($-CH_3$) groups from two adjacent BA^+ cations, collectively denoted as a BA^+ pair. Further insight into tip–sample interactions is obtained by performing constant-height imaging at varying tip–sample distances, where the contrast evolves as the tip approaches a single BA^+ pair (Fig. 4b). Corresponding force–distance (Δf–Δz) curves acquired at four representative positions—over (purple, pink) and between (green, blue) the protruding $-CH_3$ of the BA^+ chains (Fig. 4c)—reveal that the interaction becomes significantly more repulsive at sites corresponding to C–H bonds, while remaining predominantly attractive over inorganic PbI^- regions within the oscillation amplitude range. As Δz decreases, high-resolution

Open Access Article. Published on 26 March 2026. Downloaded on 6/16/2026 7:27:17 AM.
This article is licensed under a Creative Commons Attribution-NonCommercial 3.0 Unported Licence.

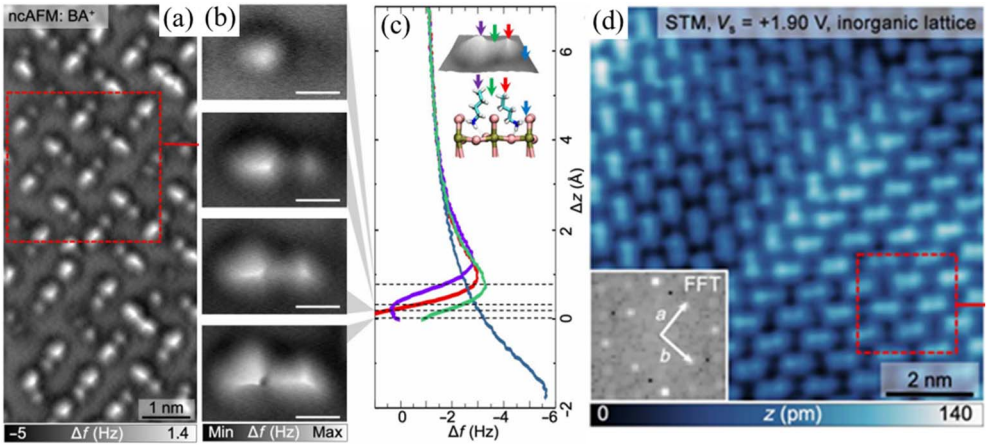

Fig. 4 (a) qPlus-AFM image of organic and inorganic layers in few-layer RPPs. (b) A group of constant-height images collected at various tip–sample distances over an individual pair of BA^+ cations. The scale bar is 0.3 nm. (c) Δf *versus* Δz curves acquired over the sites marked by color-coded arrows in the experimental 3D AFM image in the inset. (d) STM image shows the inorganic lattice of the RPPs. Reproduced from ref. 170 with permission from AAAS,[170] copyright 2022.

features associated with individual hydrogen atoms of the $-CH_3$ groups emerge, underscoring the extreme vertical sensitivity of the system.

It is worth noting that the underlying PbI^- octahedral lattice is not directly resolved in qPlus-AFM but can be identified *via* complementary STM imaging of the same region (Fig. 4d), which provides information on the inorganic sublattice. High resolution STM images can also give important information on perovskite characterization. In addition, both qPlus-AFM and STM require scanning under UHV conditions to achieve atomic-resolution imaging, and an atomically flat substrate is also a prerequisite.

2.1.2 Scanning tunneling microscopy (STM). To achieve atomic resolution, STM necessitates halide perovskites with atomically flat surfaces, as well as UHV and low-temperature environment. Two commonly adopted methods are *in situ* cleaving of bulk single crystals in vacuum,[168,171,172] and epitaxial growth of thin films *via* CVD.[63,72,166,170,173–175]

A notable example is the work of Ohmann *et al.*, who achieved atomically flat surfaces of $MAPbBr_3$ single crystals by cleaving them *in situ* under UHV.[168] The crystal was introduced into the vacuum chamber and cleaved parallel to one of its facets using a scalpel (Fig. 5a). Subsequently, it was immediately transferred into the low-temperature (T = 4.5 K) STM system without the annealing sample. The images simultaneously reveal two distinct surface domains on the (010) surface, with the protrusions identified as the Br^- anions. One domain exhibits a zigzag pattern, with perpendicularly aligned methylammonium (MA^+) that gives rise to a non-zero in-plane dipole (Fig. 5b). The other domain displays paired Br^- anions with antiparallel MA^+ alignment, yielding a net-zero dipole (Fig. 5c).[168] The spatial configuration of Br^- anions and MA^+ cations at the surface deviates from that in the bulk as shown in Fig. 5d. In particular, the MA^+ cations in the outermost layer exhibit a pronounced tilt relative to those in the bulk, indicating substantial surface reconstruction.

Beyond cleaved crystals, ultrathin epitaxial films of $MAPbI_3$ have been explored by L. M. She *et al.* The uniform $MAPbI_3$ film is approximately 10 monolayers thick on Au (111) substrates by co-depositing MAI and PbI_2 precursors in a 1 : 3 molar ratio under UHV (base pressure $\sim 10^{-10}$ mbar) at cryogenic substrate temperatures (110–130 K),[72] as shown in Fig. 5f. The STM images show well-ordered, layer-by-layer film growth (Fig. 5g). Atomic-resolution images reveal structures such as zigzag and dimerized anion arrangements (Fig. 5h and i), with halide perovskites adopting orthorhombic symmetry at low temperature.

In addition to topographic imaging, scanning tunneling spectroscopy (STS) is a powerful extension of STM that enables site-specific probing of the electronic structure. As shown in Fig. 5e and j, STS measurements on $MAPbBr_3$ single crystals and $MAPbI_3$ ultrathin films reveal markedly different electronic characteristics. In the case of $MAPbBr_3$ single crystals, the measured LDOS is dominated by occupied states, which attribute the prominent spectral features near the Fermi level to Br-derived orbitals. The MA^+ cations contribute only at deeper energy levels, and no significant contribution from Pb orbitals is observed at the surface. Subtle variations in LDOS are also evident between the zigzag and dimer domains (Fig. 5b and c).

Conversely, STS of ultrathin $MAPbI_3$ films reveals a stronger LDOS near the Fermi level (Fig. 5j), with both the conduction band minimum (CBM) and valence band maximum (VBM) clearly resolved, enabling direct extraction of the local bandgap. The reduced LDOS in the single crystal may be attributed to its greater thickness or potential interface effects arising from ambient exposure during mounting. Despite such variations, STS remains an essential tool for elucidating key electronic properties of halide perovskites, including energy-level alignment, mid-gap states, and charge localization.

Due to its capability of resolving surface structures with atomic precision, STM enables the identification of individual atomic defects.[70,172] As shown in Fig. 6a–f, STM measurements

© 2026 The Author(s). Published by the Royal Society of Chemistry

Open Access Article. Published on 26 March 2026. Downloaded on 6/16/2026 7:27:17 AM.
This article is licensed under a Creative Commons Attribution-NonCommercial 3.0 Unported Licence.

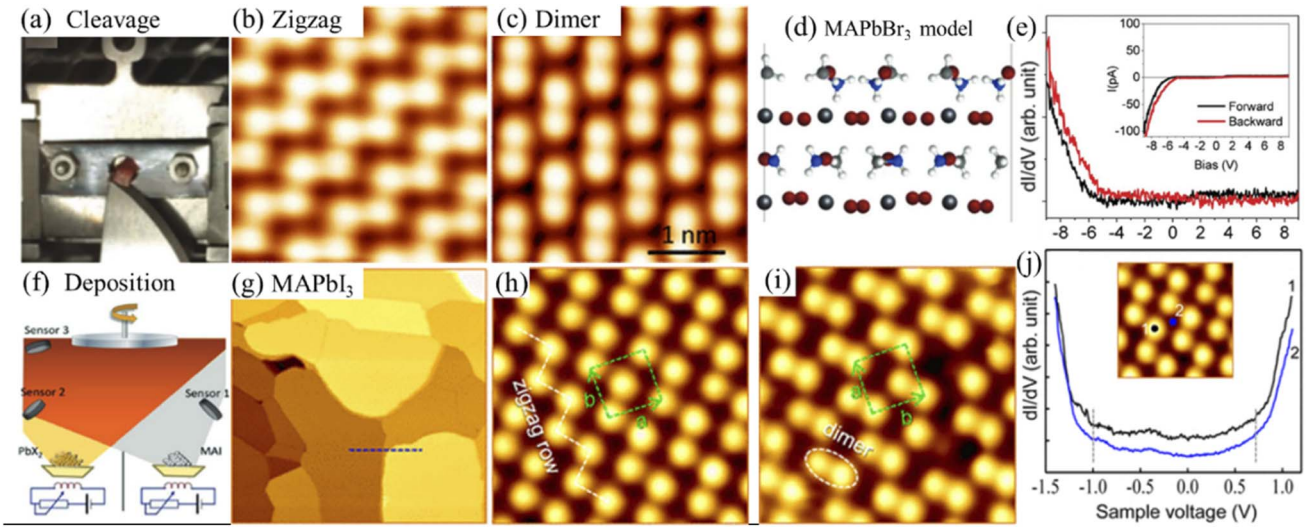

Fig. 5 (a) The single crystal cleavage for preparing halide perovskite samples. (b) Zigzag-structure and (c) dimer-structure STM images of the $MAPbBr_3$ single crystal. (d) Side view of the atomic structure model of $MAPbBr_3$. (e) d*I*/d*V* curves of $MAPbBr_3$ single crystal. Inset: corresponding current–voltage (*I*–*V*) curves. Reproduced from ref. 168 with permission from the American Chemical Society,[168] copyright 2015. (f) Chemical vapor deposition for preparing halide perovskite thin films. (g) Large-scale topographic image of flat $MAPbI_3$ ultrathin film on Au (111). (h) Zigzag-structure and (i) dimer-structure STM images of $MAPbI_3$ with atomic resolution. (j) STS at selected positions on $MAPbI_3$ ultrathin film. Reproduced from ref. 72 with permission from the American Chemical Society,[72] copyright 2016.

on $MAPbBr_3$ single-crystal surfaces allow the visualization of unpaired Br^- ions, multiple unpaired Br^- sites, as well as single, double, and triple vacancies.[172]

Moreover, high-resolution STM has been widely utilized to investigate photoinduced electronic responses of halide perovskites. As shown in Fig. 7, STM measurements performed under both dark and illuminated conditions reveal distinct modifications in the surface lattice, demonstrating that optical excitation can significantly alter surface electronic states.[171] Specifically, the surface structure evolves from a predominant dimer configuration in the dark (Fig. 7a) to a 4 × 2 superstructure under laser illumination (Fig. 7b),[171] with the corresponding orientations of MA^+ dipoles schematically represented by arrows. Furthermore, photoexcited cross-sectional STM coupled with spectroscopic analysis allows concurrent visualization of dipole alignment and electrostatic

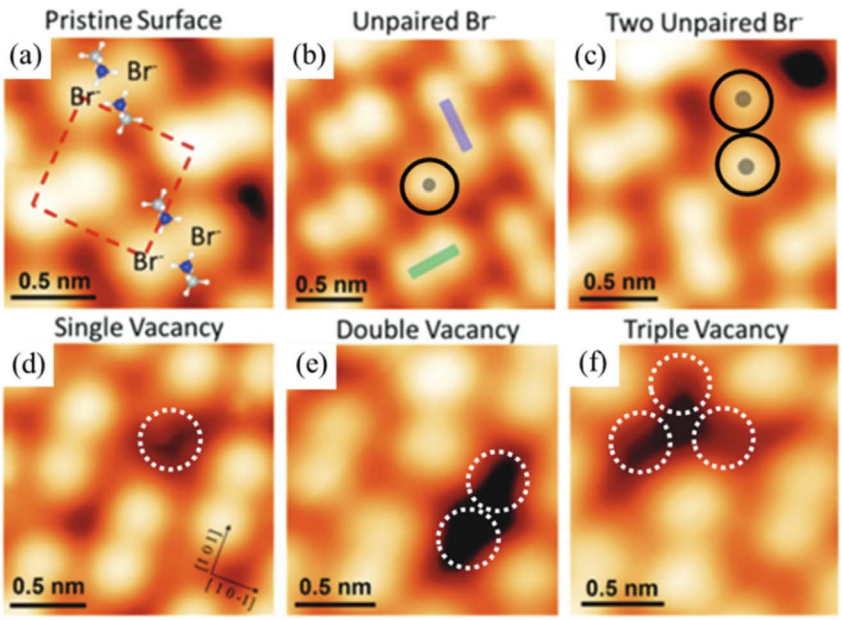

Fig. 6 STM images of defects on the surface of $MAPbBr_3$ single crystals. (a) Pristine $MAPbBr_3$ surface, bright dimer indicating Br^- portions, (b) and (c) are unpaired and two unpaired Br^- caused by lattice mismatch, (d), (e), and (f) are signal, double and triple vacancies of Br^- on the $MAPbBr_3$ surface. Reproduced from ref. 172 with permission from the American Chemical Society,[172] copyright 2019.

Open Access Article. Published on 26 March 2026. Downloaded on 6/16/2026 7:27:17 AM.
This article is licensed under a Creative Commons Attribution-NonCommercial 3.0 Unported Licence.

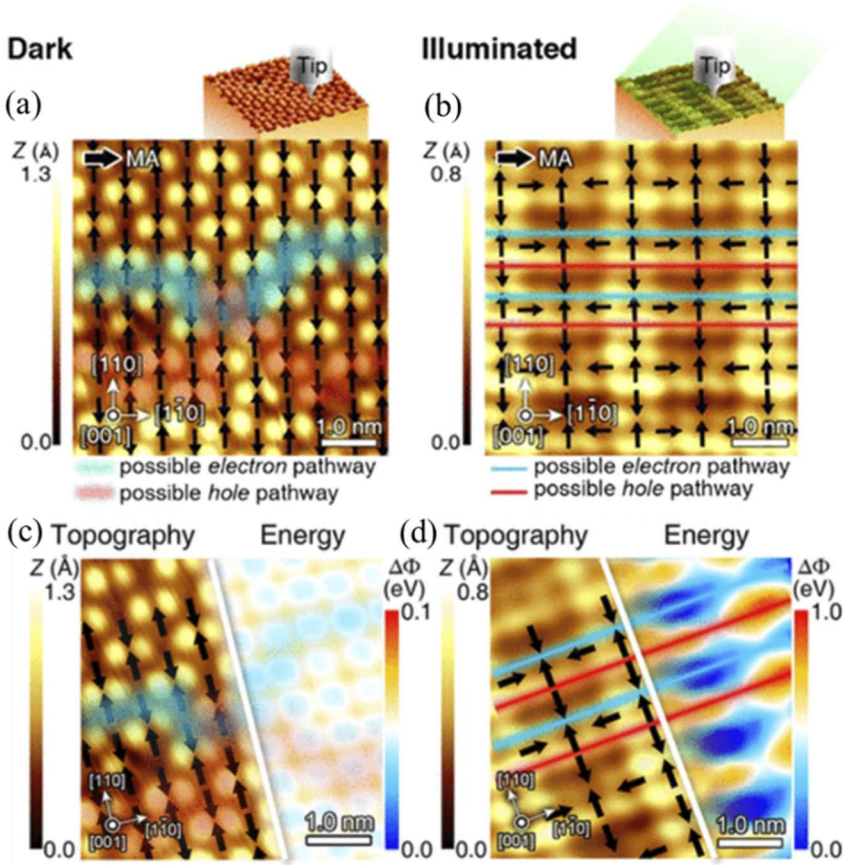

Fig. 7 (a) An STM image of cleaved $MAPbBr_3$ crystals without illumination. The dimer structure of the $PbBr^-$ octahedral lattice is observed. (b) An STM image of cleaved $MAPbBr_3$ crystals under illumination. The 4 × 2 superstructure is observed. The black arrows in (a) and (b) mark MA^+ dipole moments, which influence the possible transfer pathways of electrons and holes; (c) and (d) are corresponding electrostatic potential energy images obtained under dark and illumination conditions, respectively. Reproduced from ref. 171 with permission from the American Chemical Society,[171] copyright 2019.

potential at the atomic scale. Electrostatic potential profiles derived from κ maps, where LDOS contributions are suppressed by averaging over 2 × 1 and 1 × 1 unit cells (Fig. 7c and d), further confirm the light-induced structural transformation. Collectively, these findings provide compelling evidence for illumination-driven dipole reorganization in halide perovskites. This behavior originates from the separation of photoexcited electrons and holes in spatially displaced orbitals, resulting in a pronounced redistribution of the electrostatic potential. The ensuing dipole rearrangement gives rise to one-dimensional conduction pathways that facilitate charge transport. Remarkably, such photoinduced polarization transitions extend from the surface layers into the bulk lattice, offering a plausible explanation for both the exceptional photovoltaic efficiency and the coexistence of seemingly contradictory physical properties in halide perovskites.

For halide perovskites, STM enables direct visualization of surface reconstructions, defect configurations, and electronic inhomogeneities, which are critical for understanding and optimizing their optoelectronic performance. The ability of STM to probe LDOS and resolve changes in surface electronic structure under light excitation offers a powerful pathway to investigate light-matter interactions at the atomic level. Overall, high-resolution STM and AFM techniques are indispensable tools for perovskite related research.[176–178] Their ability to provide atomic-scale insight into structural and electronic phenomena will continue to play an increasingly important role in elucidating fundamental mechanisms and guiding the rational design of perovskite-based devices.

2.2 Nanoscale spatially resolved characterization of optoelectronic properties

Constructing and characterizing halide perovskites under UHV conditions remain technically demanding and resource intensive, particularly when aiming to preserve pristine surfaces and interfaces. While UHV-based approaches provide unparalleled insight into the intrinsic electronic structure and charge dynamics at the atomic scale, they are not always practical for routine device evaluation. In this context, measurement systems operated under ambient conditions play a crucial complementary role. Despite the reduced level of environmental control compared to UHV techniques, such systems are highly effective for assessing key device parameters, thereby

© 2026 The Author(s). Published by the Royal Society of Chemistry

Open Access Article. Published on 26 March 2026. Downloaded on 6/16/2026 7:27:17 AM.
This article is licensed under a Creative Commons Attribution-NonCommercial 3.0 Unported Licence.

bridging the gap between fundamental surface studies and practical device optimization.

2.2.1 Conductive atomic force microscopy (c-AFM). When an AFM is equipped with a conductive probe, it becomes a powerful tool for investigating the local electrical properties of halide perovskites. One of the most direct applications is *J–V* spectroscopy, which allows for spatially resolved mapping of electrical conductivity across different surface regions. By detecting current flow between the conductive tip and the sample under illumination or bias pulse, researchers can gain valuable insights into charge transport mechanisms in halide perovskites. The versatility of c-AFM also enables simultaneous acquisition of topography, friction, and electrical conductivity as a function of bias voltage. Extending this approach, photoconductive AFM (pc-AFM) incorporates illumination during measurements, using either front-side or back-side illumination of transparent substrates. Numerous studies have used pc-AFM to probe photoconductivity at grain interiors and boundaries under short-circuit conditions.[99,179–189]

A representative application is illustrated in Fig. 8, both topographic (Fig. 8a) and current maps (Fig. 8b and c) of a halide perovskite thin film were obtained by using c-AFM under illumination.[190] The photocurrent distribution reveals significant contrast between grains and GBs. The grains exhibit a positive photocurrent with an average value of approximately 16 pA without bias applied, whereas the GBs show nearly no detectable current (Fig. 8b). When a small positive bias of 0.3 V is applied, the photocurrent increases markedly to about 129 pA on average, with the signal becoming significantly stronger at the GBs than within the grains. The finding challenges the conventional view that GBs with high defect densities act predominantly as non-radiative recombination centers, which would lead to the expectation of higher photocurrent along GBs. This unexpected behavior was confirmed without and with applied bias, suggesting that GBs can act as efficient charge transport pathways once charge transfer barriers are overcome. Such barriers are attributed to band bending effects at GBs, and applying a 0.3 V voltage can significantly enhance photocurrent at these sites.

In addition, Shao *et al.* demonstrated that ion migration behavior differs markedly between grains and GBs of perovskite films.[191] Their c-AFM spectroscopy image at triangle and square marked sites in Fig. 8d under dark conditions showed significantly stronger hysteresis at GBs than within grains (Fig. 8e and f), indicating enhanced ion mobility at GBs. This behavior aligns with the hypothesis that GBs dominate ion migration in

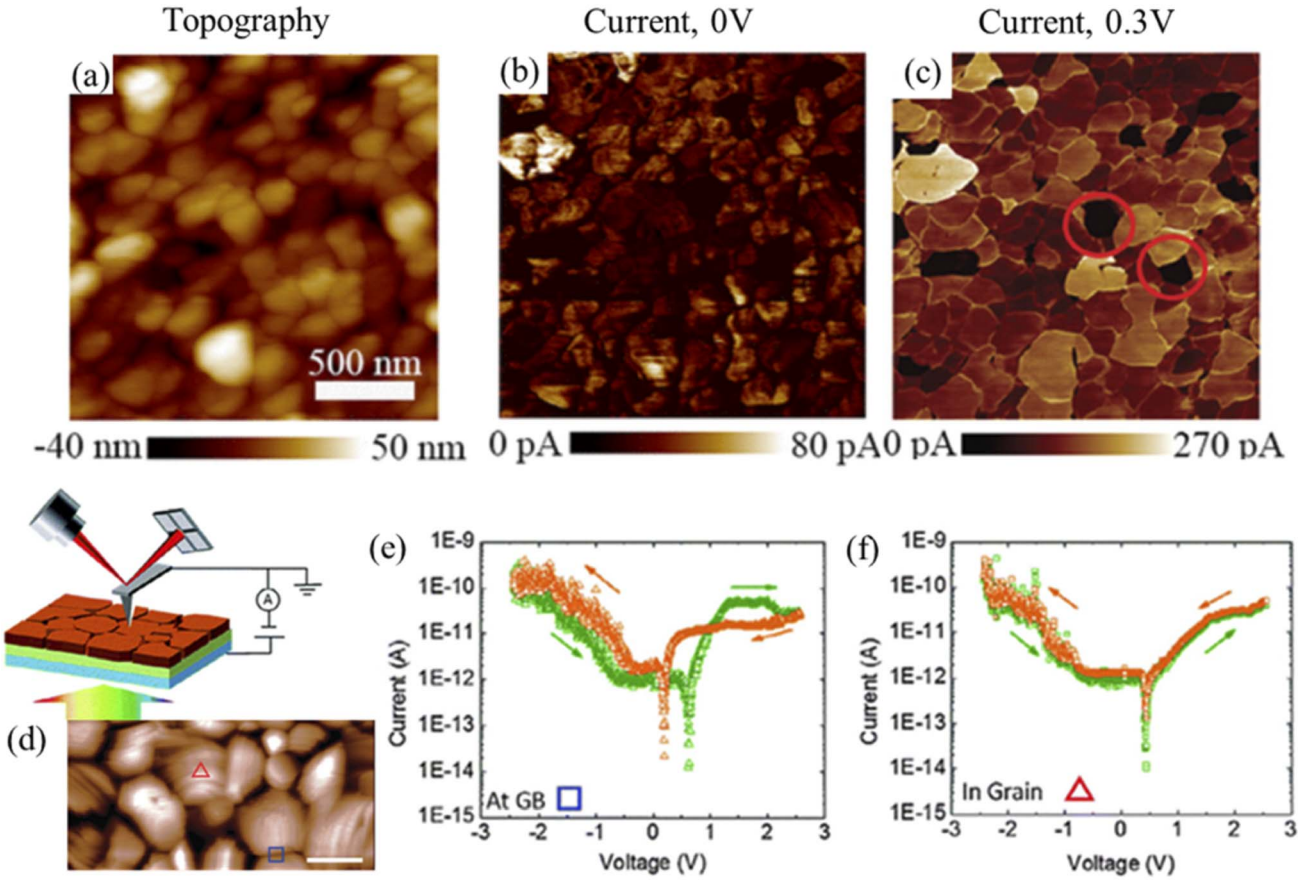

Fig. 8 (a) AFM topographic image of a $MAPbI_3$ layer and (b and c) corresponding photocurrent mapping recorded under illumination without and with +0.3 V, respectively. Reproduced from ref. 190 with permission from the American Chemical Society,[190] copyright 2015. (d) Schematic of c-AFM setup and topographic image of a $MAPbI_3$ film. The scale bar is 1 μm. (e and f) Local dark current measured at the GB and in the grain, respectively. Reproduced from ref. 191 with permission from the Royal Society of Chemistry,[191] copyright 2016.

Open Access Article. Published on 26 March 2026. Downloaded on 6/16/2026 7:27:17 AM. This article is licensed under a Creative Commons Attribution-NonCommercial 3.0 Unported Licence.

polycrystalline perovskite thin films, especially under operational conditions. Under illumination, a progressive increase in short-circuit current was observed at GBs, consistent with light-induced ion migration enhancing local conductivity. In contrast, the photocurrent at grain interiors remained relatively stable. These results further support the concept of bias-enhanced ion migration, and highlight the strong interplay between local structure, electrical bias, and ionic dynamics in halide perovskite thin films.

2.2.2 Kelvin probe force microscopy (KPFM). KPFM is one of the most widely employed techniques for characterizing surface potential and local work function variations in materials.[60,192,193] KPFM operates by detecting electrostatic forces between a conductive AFM tip and the sample surface. When two materials with different work functions are brought into close proximity, electron transfer occurs leading to the alignment of their Fermi levels and the formation of a contact potential difference (CPD) as illustrated in Fig. 9a–c. To measure the CPD, KPFM applies an external voltage consisting of both AC and DC components between the tip and the sample (Fig. 9d).[194–196] The DC bias is actively tuned in real time to nullify the electrostatic force resulting from the CPD, enabling a direct and quantitative mapping of the local surface potential. The resulting CPD image reflects spatial variations in work function across the sample surface, making KPFM particularly valuable for identifying features such as GBs, point defects, and compositional heterogeneities. When KPFM is applied to semiconductors, the interpretation of the measured surface potential becomes increasingly intricate due to inherent surface phenomena. Specifically, surface states can induce substantial band bending near the interface, leading to the formation of a space-charge region. Under such conditions, the CPD captured by KPFM represents a convolution of the material's intrinsic work function and additional electrostatic contributions originating from surface states and band bending.[194,195,197] Therefore, quantitative analysis of KPFM data on semiconductor surfaces necessitates a comprehensive evaluation of the surface electronic structure and the potential impact of surface-induced band bending.

KPFM enables spatial mapping of work-function variations in halide perovskites,[123] and provides direct correlation between local surface potential and compositional heterogeneity, such as phase separation in mixed-halide systems.[122] It has been extensively applied to halide perovskites to gain insights into lateral charge distribution and vertical energy-level alignment in multilayered device structures.[108,120,121,158,198,199] For lateral device configurations, KPFM enables mapping of carrier distribution, migration dynamics, and built-in fields in complex structures. This capability allows direct visualization of spatially resolved electrostatic potential profiles, which are critical for understanding charge separation and transport mechanisms in devices. In multilayer perovskite devices, KPFM can be employed to study vertical charge transport across different functional layers. These measurements offer crucial information on carrier transport mechanisms, interfacial charge dynamics, and energy barriers that directly impact device performance.

Given that solution-processed halide perovskite thin films typically exhibit a high density of GBs at the micrometer and submicrometer scales, lots of KPFM studies focused on investigating the role of GBs in photocarrier transport. A study combined pc-AFM and KPFM techniques to systematically investigate GBs.[198] Fig. 10a is the schematic illustration of pc-AFM for characterization of polycrystalline $MAPbI_3$ thin film deposited on FTO, a light is illuminated at the back side of the device. Fig. 10b and c show topography and CPD images of the $MAPbI_3$ thin film, respectively, acquired in a single KPFM measurement. The clear surface potential difference between GBs and grains is revealed in the CPD image. The built-in potential at GBs may facilitate selective carrier extraction and suppress electron–hole recombination. This is often interpreted as evidence of favorable electric fields that promote selective charge extraction.

The relationship between SPV and work function variations in $FAPbI_3$ and $(FA_{0.8}Cs_{0.2})PbI_3$ films was examined using KPFM with and without illumination (Fig. 10d and e).[123] Upon illumination, the $(FA_{0.8}Cs_{0.2})PbI_3$ film displayed a much more significant work function shift than the modest change observed in the $FAPbI_3$ (Fig. 10f). This difference in electronic

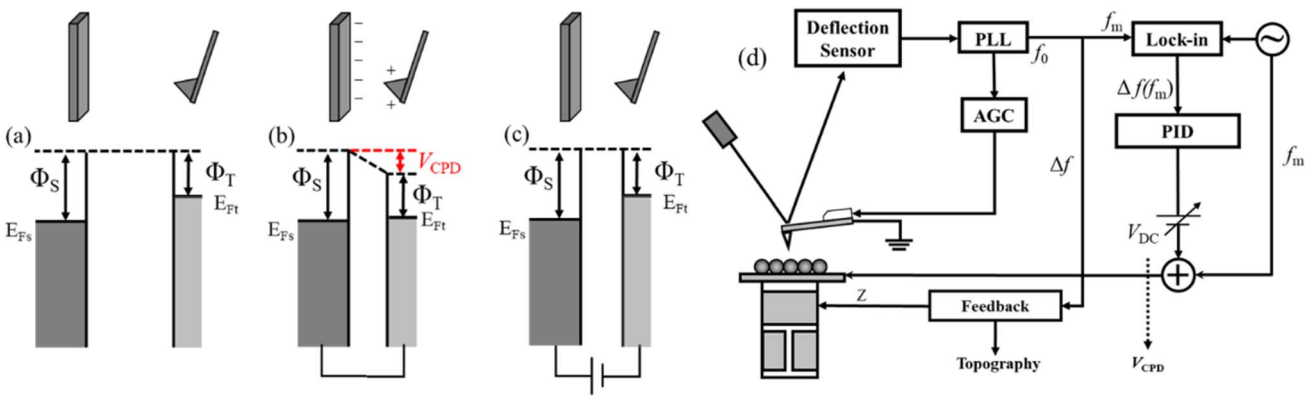

Fig. 9 (a–c) Principle of CPD measurement based on KPFM. (d) Schematic of the KPFM setup. Reproduced from ref. 195 with permission from Elsevier,[195] copyright 2024.

© 2026 The Author(s). Published by the Royal Society of Chemistry

Open Access Article. Published on 26 March 2026. Downloaded on 6/16/2026 7:27:17 AM.
This article is licensed under a Creative Commons Attribution-NonCommercial 3.0 Unported Licence.

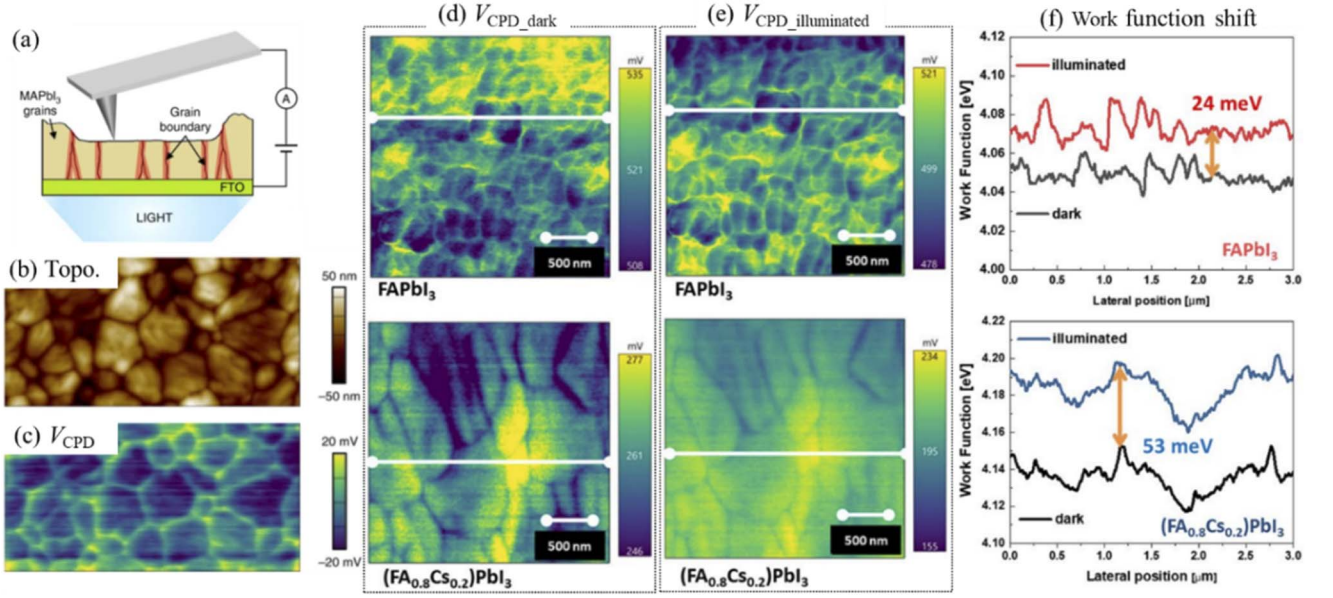

Fig. 10 (a) Schematic illustration of bottom-illuminated pc-AFM for characterizing polycrystalline $MAPbI_3$ thin films. (b) Topographic and (c) CPD images of $MAPbI_3$ thin film obtained by KPFM simultaneously. The size of images (b and c) is 3 μm × 6 μm. Reproduced from ref. 198 with permission from Springer Nature,[198] copyright 2020. (d and e) V_{CPD} images of $FAPbI_3$ and $(FA_{0.8}Cs_{0.2})PbI_3$ films obtained by KPFM under dark and illuminated conditions. (f) The correlated work function recorded along the marked line in (d and e), arrows marked the work function shift between dark and illuminated conditions for each film. Reproduced from ref. 123 with permission from Springer Nature,[123] copyright 2026.

behavior is closely linked to the structural improvement of the perovskite lattice. As a result, the larger work function shift in $(FA_{0.8}Cs_{0.2})PbI_3$ indicates that the Fermi level moves deeper toward the valence band. This shift represents an optimized energy alignment with the HTL, facilitating more efficient charge extraction at the interface. Ultimately, these findings confirm that Cs^+ substitution is an effective strategy to reduce defect-related recombination and improve the overall energy landscape of the device.

One of the most intriguing phenomena in perovskite-based devices is the presence of photocurrent hysteresis, which is widely believed to stem from ion migration under external bias or illumination conditions.[49] The hysteresis has been linked to dynamic changes in internal electric fields and local doping states, both of which can be effectively studied using KPFM. For example, Yuan *et al.* demonstrated that ion migration leads to local chemical doping in perovskite films, causing significant variations in surface potential before and after electrical poling, as captured by KPFM measurements (Fig. 11a–c).[158] Under an applied electric field, mobile ions within the $MAPbI_3$ layer redistribute and modulate the local electronic environment: the accumulation of MA^+ vacancies near the anode can lead to p-type doping by attracting holes to maintain charge neutrality in the film, whereas the accumulation of MA^+ ions near the cathode induces n-type doping (Fig. 11c). These doping-induced changes shift the Fermi level locally and alter band bending at the contacts, thereby influencing the separation, transport, and extraction of photogenerated carriers. In this way, KPFM serves as a powerful tool to reveal the spatial and temporal evolution of internal electric fields in operating perovskite-based devices.

In a comprehensive study conducted by Yun *et al.*, a positive or negative bias was applied to the perovskite surface, and subsequently, the surface potential was mapped by KPFM (Fig. 11d–i).[108] They conducted studies on a $(FAPbI_3)_{0.85}(MAPbI_3)_{0.15}/TiO_2/FTO$ sample and in ambient air. When no bias was applied to the perovskite surface, the normal CPD images are shown in Fig. 11e and h. When the perovskite surface is poled with a positive bias, a higher CPD (lower work function) is observed at the GBs than in grain interiors (Fig. 11f), indicative of the upward band bending or a potential barrier for electrons. In contrast, when the surface is polled with negative (Fig. 11i) bias, a lower CPD (higher work function) is observed at GBs than in the grain interior, indicative of the downward band bending or a potential well for electrons. The results were attributed to migration of positively and negatively charged ions within the GBs that correspond to preferred pathways for ions to migrate in the perovskite film.

The operational stability of mixed-halide perovskites is severely compromised by light-activated phase segregation, a phenomenon that induces detrimental bandgap narrowing. Mechanistic investigations have closely linked this spatially heterogeneous degradation to the accumulation of positive space charges at GBs. For instance, Yun and colleagues observed that the GBs in $(FAPbI_3)_{0.85}(MAPbBr_3)_{0.15}$ films display a noticeably depressed surface potential compared to grain interiors.[108] Tang *et al.* further elucidated this topography-dependent behavior, demonstrating that GBs serve as the primary nucleation sites for iodide-rich clusters.[122] Characterized by a localized minimum in the bandgap, these segregated

Open Access Article. Published on 26 March 2026. Downloaded on 6/16/2026 7:27:17 AM.
This article is licensed under a Creative Commons Attribution-NonCommercial 3.0 Unported Licence.

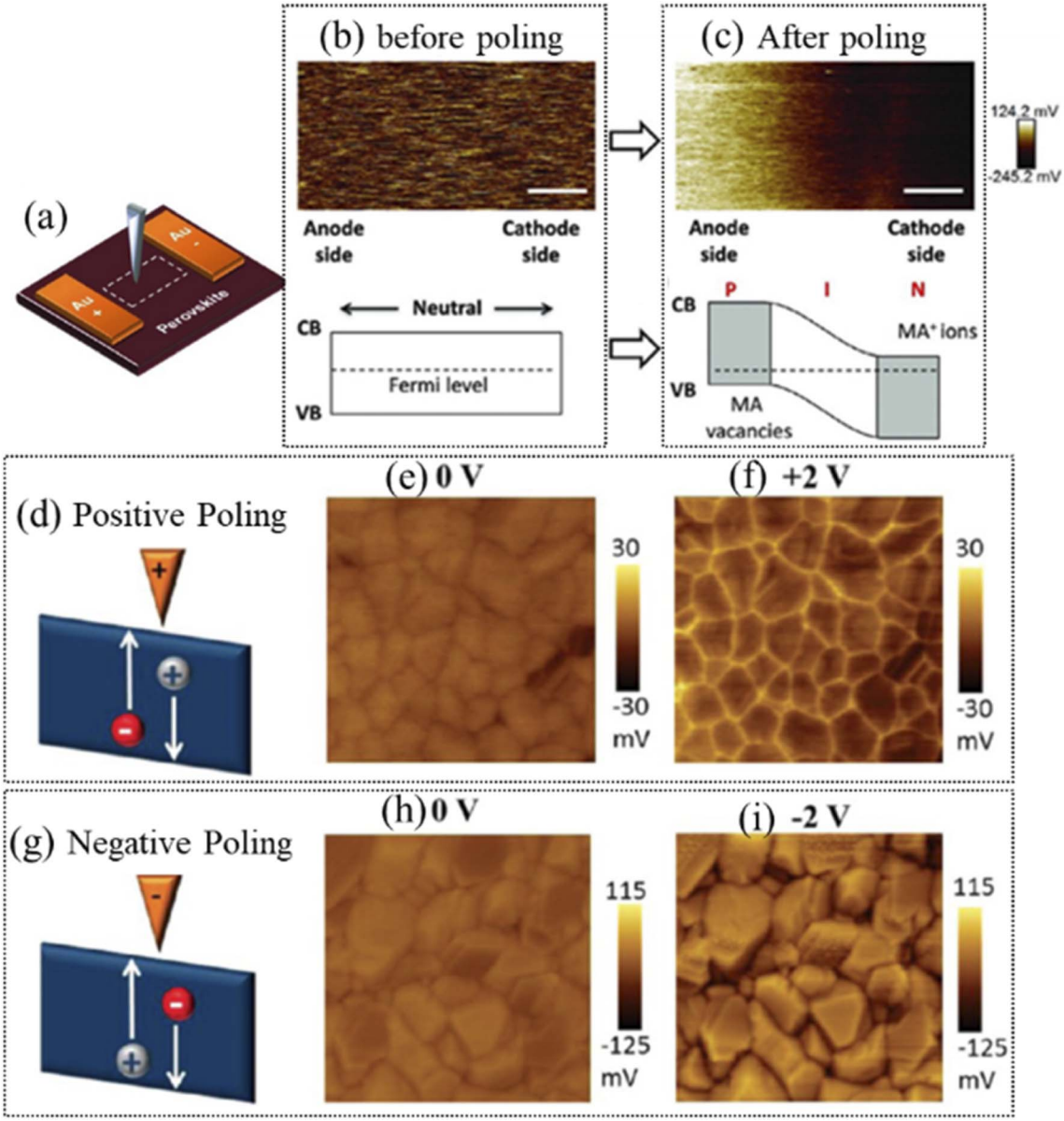

Fig. 11 (a) Schematic of the KPFM measurements of the lateral structure devices. (b) KPFM potential images and corresponding energy diagram of $MAPbI_3$ films between the two Au electrodes before and (c) after electrical poling, respectively. The scale bar is 6 μm. Reproduced from ref. 158 with permission from Wiley-VCH GmbH,[158] copyright 2015. (d) Schematic of electron and hole polarization in KPFM measurement when a positive tip bias is applied to the perovskite surface. CPD images at (e) 0 V and (f) +2 V tip bias with a 4 μm^2 region. (g) Schematic of electron and hole polarization in KPFM measurement when a negative tip bias is applied to the perovskite surface. CPD images at (h) 0 V and (i) −2 V tip bias with a 4 μm^2 region. Reproduced from ref. 108 with permission from Wiley-VCH GmbH,[108] copyright 2016.

domains act as charge recombination centers, ultimately causing the characteristic red-shift in PL emission.

To probe the underlying electrostatic origins, spatially resolved KPFM was utilized to map the surface potential of $CH_3NH_3PbBr_{0.9}I_{2.1}$ films (Fig. 12a and b). The extracted spatial potential profiles confirmed a pronounced upward band bending at the structural interfaces (Fig. 12c), verifying an elevated density of localized positive charges. This unique electrostatic environment underpins a dynamic halide migration model (Fig. 12d). Upon photoexcitation, the accumulated positive charges at the boundaries create a strong local electric field, selectively drawing mobile iodide ions toward the interfaces to achieve charge compensation. These results suggest that the higher concentration of positive space charge near the GBs may provide the initial driving force for phase segregation.

For multilayer perovskite-based devices, KPFM can be employed to study internal potential and coupled ionic–electronic transport across different functional layers.[15,109,120,121,199,200] To enable such cross-sectional investigations, the device must be cleaved laterally to expose a clean, unpolished side surface, allowing access to the internal interfaces with minimal damage or distortion. As illustrated in

 © 2026 The Author(s). Published by the Royal Society of Chemistry

Open Access Article. Published on 26 March 2026. Downloaded on 6/16/2026 7:27:17 AM.
This article is licensed under a Creative Commons Attribution-NonCommercial 3.0 Unported Licence.

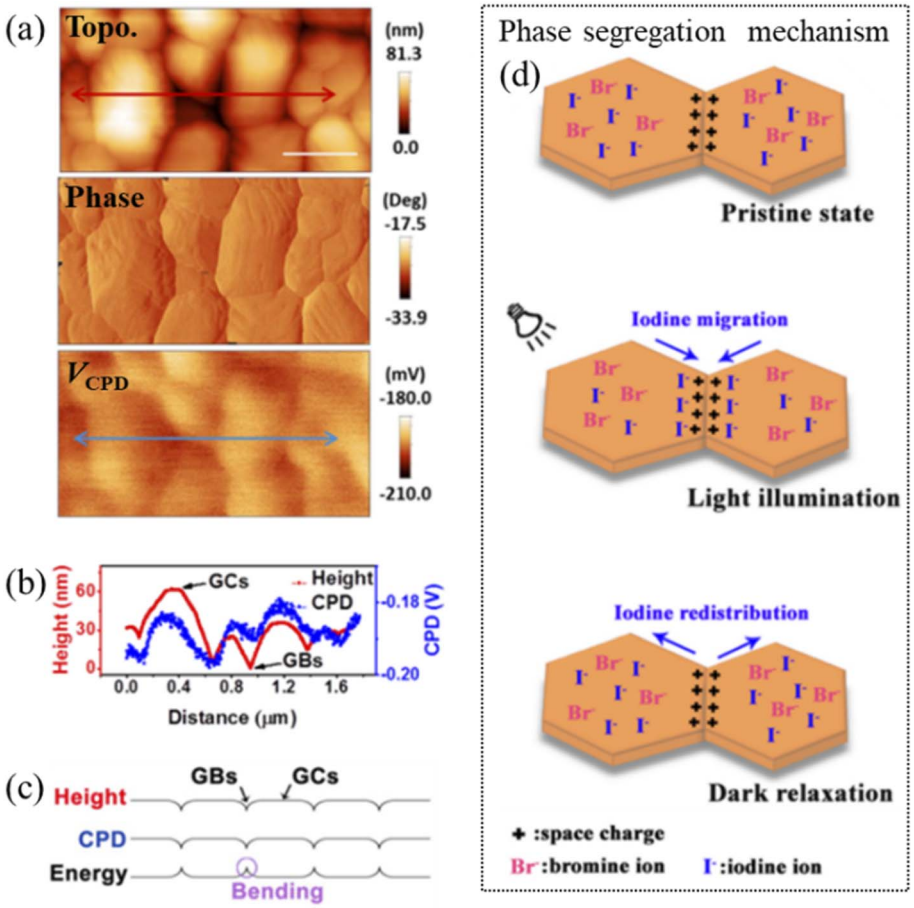

Fig. 12 (a) Topography, phase, and V_{CPD} images of $CH_3NH_3PbBr_{0.9}I_{2.1}$. (b) Corresponding profile along lines marked in topography and V_{CPD} images. (c) Energy alignment between GBs and grains. (d) Schematic illustration of the possible mechanism for phase segregation at the GBs. Reproduced from ref. 122 with permission from the American Chemical Society,[122] copyright 2018.

Fig. 13a, the KPFM setup involves scanning a Pt/Ir-coated AFM tip along the exposed cross-section of the device, which is $MAPbI_3/TiO_2$ on the Si substrate. This configuration enables simultaneous acquisition of topography and surface potential images, with nanometer-scale spatial resolution.[109] Fig. 13b shows the KPFM cross-section images; surface potential exhibits gradient changes across different material surfaces. Fig. 13c shows the CPD statistical distribution of Fig. 13b, a CPD variation of 155 mV was determined between metal oxides and the perovskite layer. These variations are mainly due to the nanostructure and inhomogeneous surface of the measured materials which entail a high amount of defect states. Fig. 13d shows a schematic band diagram for the case of positive charge accumulation (hole traps) at the GB. It is possible to calculate the width of the barrier potential at the GBs using known barrier models provided GB is of negligible width compared to the grain size. This model was used to analyze GBs in p-type polycrystalline silicon, II–VI semiconductors and chalcopyrite materials.[201,202] Importantly, the voltage drops across the entire stack is governed by the equivalent series resistance of each layer and interface. Variations in potential drop among different interfaces reflect the relative strengths of their charge transport barriers. This method enables identification of rate-limiting interfaces and the detection of interfacial asymmetries. However, it is worth noting that absolute potential comparisons across devices can be complicated by artifacts such as minor edge shunting introduced during cleaving, which may prevent the full applied voltage from being distributed across the entire stack.

Otherwise, there are reports on independently applied cross-sectional KPFM to perovskite-based devices incorporating either $CH_3NH_3PbI_{3-x}Cl_x$ (ref. 200) or $CH_3NH_3PbI_3$ (ref. 120 and 121) as the absorber layer; TiO_2 and Spiro-OMeTAD were employed as the electron and hole transport layers, respectively. Notably, in-dark KPFM measurements on $CH_3NH_3PbI_{3-x}Cl_x$ films deposited on compact TiO_2 substrates revealed the presence of a non-uniform internal electric field across the perovskite layer.[200] The authors attributed this gradient to a carrier depletion region extending over approximately half the film thickness, consistent with a p–n heterojunction model. In contrast, Bergmann *et al.* reported uniform electric field distributions throughout the $CH_3NH_3PbI_3$ absorber layer when deposited on mesoporous TiO_2, suggesting a p–i–n junction behavior instead.[121] This discrepancy highlights the critical influence of substrate morphology and interface quality on the internal electrostatics of perovskite-based devices.

Open Access Article. Published on 26 March 2026. Downloaded on 6/16/2026 7:27:17 AM.
This article is licensed under a Creative Commons Attribution-NonCommercial 3.0 Unported Licence.

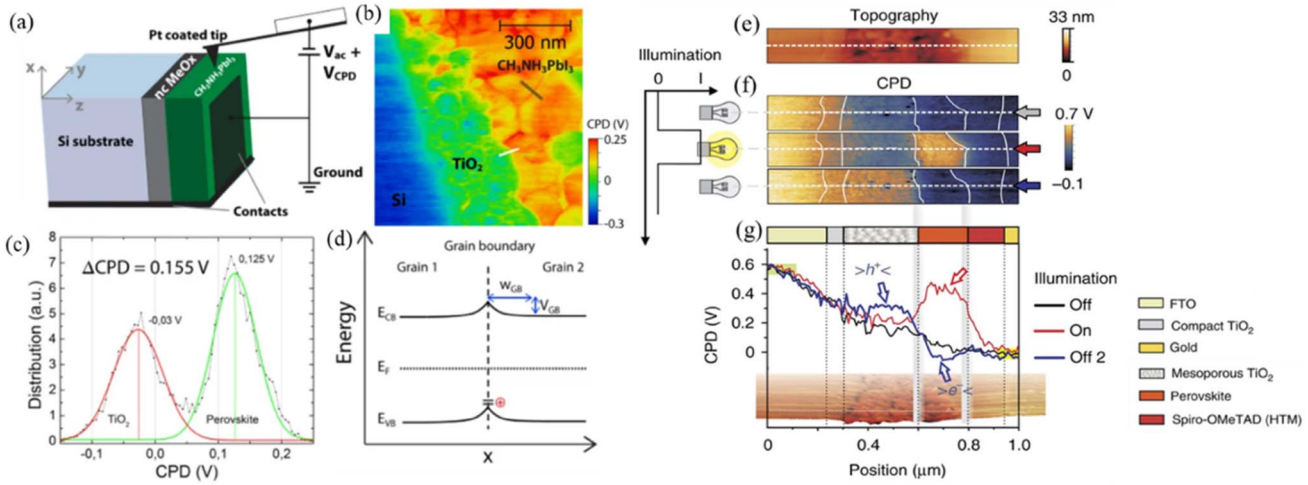

Fig. 13 (a) Schematic illustration of the cross-section KPFM measurement setup. (b) KPFM image showing cross-sections of $MAPbI_3/TiO_2$ deposited on a Si substrate. (c) CPD statistical distribution for the CPD image of the $MAPbI_3/TiO_2$ interface. (d) The electronic band structure at the GBs where the potential is slightly higher (more p-type) compared to the grain interior. Reproduced from ref. 109 with permission from Springer Nature,[109] copyright 2015. (e) AFM topographic image, (f) CPD maps recorded under short-circuit conditions before illumination, under illumination, and after turning the illumination off of a perovskite solar cell. (g) Line profiles extracted from the CPD maps. Reproduced from ref. 120 with permission from Springer Nature,[120] copyright 2014.

Furthermore, Bergmann *et al.* extended their investigation to illuminated short-circuit conditions.[120] Cross-sectional CPD maps revealed positive surface potential shifts within the perovskite layer under illumination (Fig. 13e–g), which were interpreted as the result of unbalanced electron–hole extraction. The increase in potential after turning on the illumination reveals an accumulation of holes inside the perovskite layer. The comparison between the initial dark profile and the one recorded after switching off the illumination reveals the existence of trapped holes and electrons inside the mesoporous TiO_2 and the perovskite film, respectively. Additionally, trapped charge carriers were evidenced by residual surface potential changes recorded immediately after turning off light.

These findings collectively underscore the utility of cross-sectional KPFM in resolving spatial variations in band bending, electric field distribution, and carrier dynamics across multilayered perovskite-based device stacks. Importantly, the method enables visualization of device asymmetries, transport bottlenecks, and interfacial charge accumulation that are otherwise invisible to traditional electrical measurements. However, as with any technique involving cleaved cross-sections, care must be taken to minimize edge artifacts and sample damage, which can influence potential profiles and complicate quantitative interpretation. Nevertheless, cross-sectional KPFM remains an indispensable tool for understanding the internal physics of perovskite-based devices and for guiding interface engineering and device optimization.

Despite these experimental insights, achieving atomic-scale resolution with KPFM remains highly challenging. Although short-range electrostatic forces could, in principle, yield atomic-level contrast in CPD, the measurements are frequently affected by a range of non-electrostatic artifacts, including tip asymmetry, chemical interactions between tip and sample, and cantilever dynamics. In semiconductors like perovskites, additional complications arise from the electric-field-induced redistribution of surface carriers, which can obscure the intrinsic work function contrast. Nonetheless, the local perturbation caused by the AFM tip can become a tool. Tip-induced charge transfer has emerged as a powerful approach for probing carrier dynamics, trap states, and nanoscale electronic inhomogeneity. These capabilities open up exciting possibilities for bottom-up material design, particularly in the context of atomic-scale fabrication and functional interface engineering. With continued advances in tip design, signal modeling, and noise suppression, KPFM and related electrostatic scanning probe techniques may soon enable quantitative and high-resolution analysis of complex perovskite-based heterostructures at the ultimate nanoscale limit.

It is noteworthy that when measurements are performed on perovskite-based devices under ambient conditions, such as in pc-AFM or KPFM experiments, the requirement for flat surfaces is much less strict than for UHV-based atomic-resolution characterization. Instead, the overall device structure becomes a key factor, as the measured signals typically originate from functional device structures rather than idealized, perfect surfaces. Consequently, samples are frequently prepared as complete device configurations to ensure that the observed electrical or optoelectronic responses accurately reflect the actual working processes of the device.

A further important consideration relates to the potential influence of surface degradation during the measurement. Halide perovskites are naturally sensitive to environmental factors, including moisture, oxygen, and long-term light illumination, all of which can significantly change the surface chemical composition and electronic structure. As a result, the measured topography, local conductivity, or surface potential

© 2026 The Author(s). Published by the Royal Society of Chemistry

Open Access Article. Published on 26 March 2026. Downloaded on 6/16/2026 7:27:17 AM. This article is licensed under a Creative Commons Attribution-NonCommercial 3.0 Unported Licence.

may change during the experiment, potentially introducing measurement errors or artifacts. To avoid these issues, SPM measurements are often conducted in controlled environments, such as inert gas atmospheres or glovebox conditions, with careful regulation of light intensity and measurement duration. This rigorous approach helps minimize environmental degradation and improves the reliability and reproducibility of the experimental data.

3 Extensions of scanning probe microscopy for halide perovskites

The aforementioned SPM-based approaches with illumination provide a preliminary means to investigate the light response of perovskite-based devices under conditions resembling natural light exposure. However, these methods typically lack advanced optical measurement capabilities and therefore yield limited information regarding the detailed optoelectronic behavior of the material. The SPM tip can serve as a precise tool for guiding and localizing laser excitation, enabling spatially resolved optical characterization of material surfaces. This section has introduced a range of advanced characterization techniques based on extensions of SPM, highlighting the use of state-of-the-art optoelectronic detection strategies. Such hybrid approaches significantly enhance the capability to probe the nanoscale optical and electronic properties of halide perovskites with high spatial resolution.

3.1 Scanning near-field optical microscopy (SNOM) and photoluminescence-AFM (PL-AFM)

SNOM enables optical imaging beyond the diffraction limit by exploiting fields confined within tens of nanometers from the sample surface. Depending on the configuration, SNOM uses either a subwavelength aperture or a sharp metallic tip to scatter near-field signal, achieving spatial resolutions of ~20–100 nm.[151,152] Building on the SNOM setup, PL-AFM is a hybrid technique that integrates AFM with nanoscale-resolved PL imaging. Compared to conventional confocal PL microscopy (spatial resolution ~200–300 nm), PL-AFM offers significantly improved resolution, making it well-suited for studying nanoscale optoelectronic inhomogeneities.[150] This precision is crucial for optimizing device efficiency through improved understanding of charge carrier dynamics. By locally exciting the sample with a focused laser and detecting the emitted PL through a transparent tip or external optics, PL-AFM allows simultaneous mapping of topography and optical emission with sub-50 nm resolution. These techniques have been extensively applied to halide perovskite materials to investigate nanoscale optical heterogeneities.[150,158,159] For example, PL mapping of $MAPbBr_3$ and $MAPbI_3$ thin films has revealed "hot spots" of enhanced emission correlated with regions of higher crystallinity, underscoring the correlation between structural order and radiative efficiency.[150] Such high-resolution PL maps provide valuable insights into local carrier dynamics and recombination behavior that are otherwise averaged out in bulk measurements.

In particular, PL-AFM is effective for identifying non-radiative recombination centers associated with GBs, voids, and strain. Researchers demonstrated that PL quenching occurs preferentially at GBs in perovskite films, indicating elevated defect densities and trap-assisted recombination.[150] In Fig. 14a, $CH_3NH_3PbI_3$ perovskite films were excited using a continuous wave laser ($\lambda_{exc} = 405$ nm) in a PL-AFM setup. The PL emission was collected in transmission mode with confocal geometry. PL maps were corrected for small differences in absorption by measuring the transmitted excitation laser intensity. Localized spatial variations in PL intensity up to a factor of 2.6 are observed, which do not show a correlation with features in topography (Fig. 14b and c). Representative transient PL decays taken in spatial regions of high (red) and low (blue) PL intensity, measured in a confocal microscope configuration with ≈250 nm resolution for $CH_3NH_3PbI_3$ samples on glass (Fig. 14d). The PL lifetime of the perovskite in the high PL intensity region is significantly larger than that in the low PL intensity region. It means slower non-radiative recombination kinetics in regions of high emission intensity, compared to regions of lower intensity. Time constants of PL decays were determined by the drop of emission intensity to $1/e$ for $CH_3NH_3PbI_3$. Besides, the PL emission peak of the perovskite in the high PL intensity region is narrower than that in the low PL intensity region (Fig. 14e). Fig. 14f shows the spatial distribution of the PL emission peak's full width at half maximum (FWHM), extracted from locally recorded PL spectra of $CH_3NH_3PbI_3$ samples. The red regions indicate areas with high PL intensity and smaller FWHM values, whereas the white regions correspond to voids in the film. The reduced FWHM in the high-intensity regions is likely associated with improved crystallinity, resulting in a narrower distribution of electronic energy levels.

These findings highlight the strength of PL-AFM in elucidating the structure-dependent optoelectronic properties. However, PL-AFM requires precise optical alignment and stability against thermal drift and tip–sample interaction artifacts. The limited excitation and detection volume can also reduce signal intensity, necessitating careful optimization of experimental parameters.

3.2 Photothermal-induced resonance (PTIR) and atomic force microscopy-infrared spectroscopy (AFM-IR)

PTIR and AFM-IR are two powerful hybrid techniques that combine the high spatial resolution of AFM with the molecular specificity of infrared absorption spectroscopy. Both methods operate on the principle of detecting localized photothermal expansion triggered by pulsed and tunable IR laser excitation. This approach enables nanoscale vibrational spectroscopy with lateral resolutions of approximately 10–20 nm, far surpassing the diffraction limit inherent to conventional IR spectroscopy.

In a typical AFM-IR configuration, IR absorption within the sample generates localized thermal expansion, which, in turn, excites oscillations of an AFM cantilever operating in contact mode. By monitoring the cantilever's resonant amplitude or phase as a function of the IR wavelength, one can obtain site-

Open Access Article. Published on 26 March 2026. Downloaded on 6/16/2026 7:27:17 AM.
This article is licensed under a Creative Commons Attribution-NonCommercial 3.0 Unported Licence.

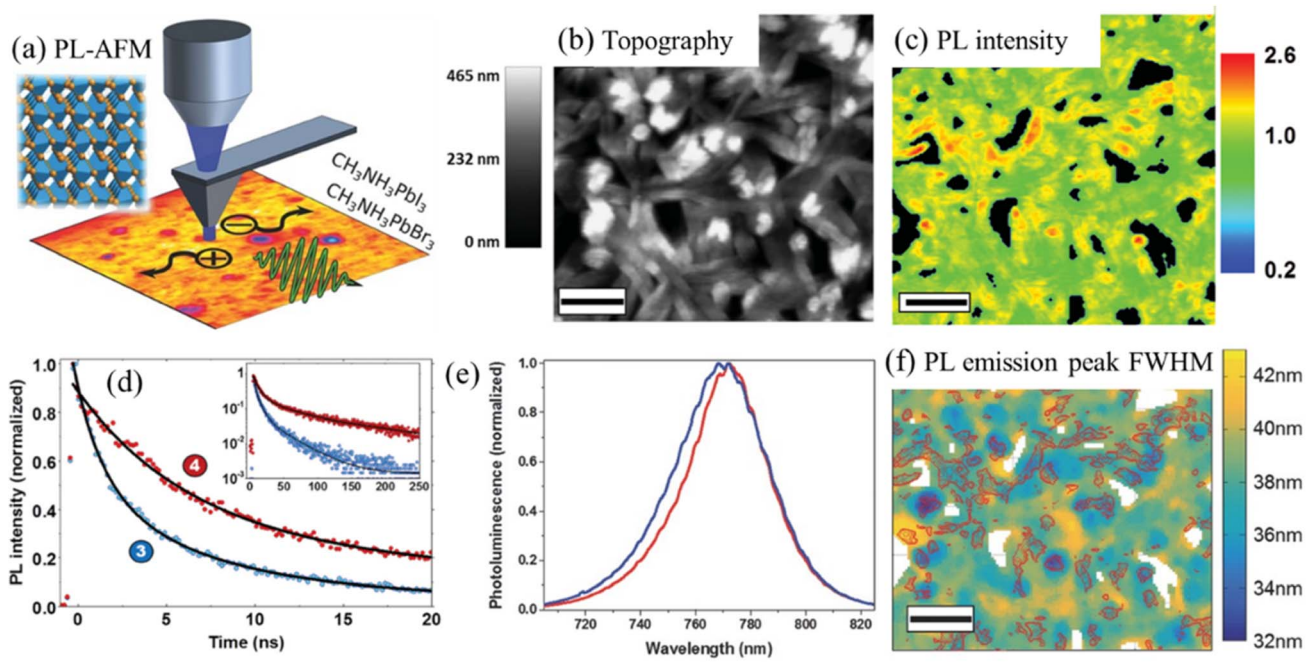

Fig. 14 (a) Schematic illustration of the PL-AFM measurement setup. A PL laser was guided through the tip. (b) Topography and (c) map of the ratio between locally detected *versus* spatially averaged PL intensity for spin-coated $CH_3NH_3PbI_3$ perovskite thin-films on glass. The scale bar is 4 μm. (d) Representative transient PL decays taken in spatial regions of high (red) and low (blue) photoluminescence intensity, measured in a confocal microscope configuration with ≈250 nm resolution. Insets show the transient PL decays on logarithmic scale for longer time delays. (e) Representative PL emission spectra averaged over regions of high and low photoluminescence intensity $CH_3NH_3PbI_3$ samples. (f) The spatial distribution of the photoluminescence emission FWHM was determined from locally recorded PL spectra for $CH_3NH_3PbI_3$ samples. The scale bar is 4 μm. Reproduced from ref. 150 with permission from Wiley-VCH GmbH,[150] copyright 2015.

specific absorption spectra comparable in spectral quality to those from Fourier-transform infrared spectroscopy (FTIR), yet with nanometric spatial resolution. Consequently, AFM-IR is particularly effective for characterizing flat, IR-transparent, or weakly absorbing materials, making it especially suitable for the chemical and structural analysis of thin-film systems.

In contrast, PTIR detects cantilever deflection instead of resonant oscillation, thus offering greater flexibility in experimental geometry.[160,161] Moreover, PTIR can operate in reflection mode, which makes it ideally suited for investigating opaque, highly scattering, or structurally complex samples, such as buried interfaces and multilayer architecture. Typically, the sample is placed on an IR-transparent prism and illuminated from below, and absorption spectra are collected point-by-point as the laser wavelength is tuned. Furthermore, recent developments have extended PTIR beyond the traditional IR spectral range by incorporating alternative excitation sources and optical geometries, thereby broadening its applicability to a wide range of material systems.[203]

Both AFM-IR and PTIR have proven indispensable for probing chemical and structural heterogeneity in halide perovskites. These materials exhibit pronounced nanoscale variations in composition, phase, and ionic distribution, all of which critically influence their optoelectronic performance and long-term stability. For instance, AFM-IR has been employed to detect local variations in the iodine-to-lead (I/Pb) ratio under external stimuli, providing direct nanoscale evidence of halide ion migration.[160] This migration behavior can be attributed to the relatively low activation energy of halide ion transport compared with that of metallic cations.

A compelling demonstration of the potential of PTIR was reported in the study of $MAPbI_{3-x}Cl_x$ perovskite thin films, where PTIR was employed to map the spatial distribution of chlorine both before and after thermal annealing.[161] As illustrated in Fig. 15, the combination of AFM topography, PTIR chemical maps, and site-specific absorption spectra revealed pronounced nanoscale heterogeneity prior to annealing. Specifically, PTIR signals measured near the bandgap edge distinguished Cl-rich (blue) and Cl-deficient (red) domains, highlighting compositional variations that were further confirmed by localized infrared spectra. As the photon energy increases from the band-edge region (702 nm, Fig. 15c), the absorption ratio maps of the initial sample display a gradual reduction in contrast, indicating a decrease in optical heterogeneity. This trend implies that the bandgap of the as-prepared $MAPbI_{3-x}Cl_x$ film is spatially non-uniform, which likely reflects localized fluctuations in both chemical composition and crystallographic lattice parameters. Taken together, these findings provided direct nanoscale evidence of thermally induced halide migration and clarified the debated role of chlorine in perovskite crystallization, film morphology, and optoelectronic quality.

Beyond compositional analysis, PTIR has also proven highly effective in probing dynamic processes such as lateral ion

© 2026 The Author(s). Published by the Royal Society of Chemistry

Open Access Article. Published on 26 March 2026. Downloaded on 6/16/2026 7:27:17 AM.
This article is licensed under a Creative Commons Attribution-NonCommercial 3.0 Unported Licence.

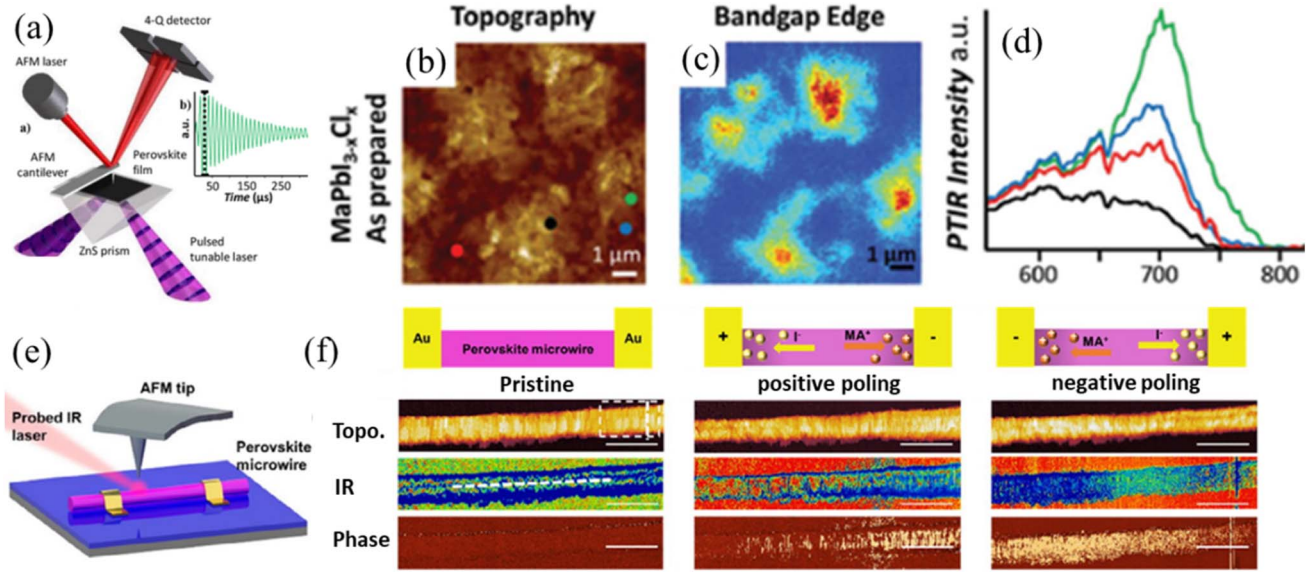

Fig. 15 (a) Schematic illustration of the PTIR experimental setup. If the sample absorbs the laser pulses (discs in purple cones), it rapidly expands deflecting the AFM cantilever whose position is monitored by the four-quadrant detector. Mapping of chlorine distribution in the $MAPbI_{3-x}Cl_x$ perovskite monitored by PTIR. (b) AFM height topographic images of an $MAPbI_{3-x}Cl_x$ film. (c) The corresponding PTIR absorption maps obtained by illuminating the sample at the bandgap edge (1.77 eV). (d) The PTIR absorption spectra obtained at the location of the red, dark, blue, and green dots in (b). Reproduced from ref. 161 with permission from the American Chemical Society,[161] copyright 2015. (e) Schematic illustration of the AFM-IR system. (f) Infrared near-field mapping images (AFM images, near-field optical images, and phase images) for a perovskite microwire under pristine, positive poling, and negative poling conditions. The scale bar is 500 nm. Reproduced from ref. 160 with permission from the American Chemical Society,[160] copyright 2016.

migration and interfacial polarization under light illumination or electrical bias.[161] By detecting the localized photothermal response associated with ionic motion, PTIR enables direct observation of these transient behaviors under realistic operating conditions. Consequently, this technique has emerged as a powerful spectroscopic tool for elucidating degradation mechanisms including ion migration, trap formation, and chemical instability.

In a complementary investigation, Zhang *et al.* employed spatially resolved vibrational and optical spectroscopy to visualize ion migration in perovskite microwires.[160] As shown in Fig. 15e, a schematic of the AFM-IR configuration integrated within a scattering-SNOM system was used, where a constant bias was applied between source and drain electrodes (Fig. 15f) to simulate the poling field in perovskite solar cells. The AFM, near-field optical, and phase images revealed distinct electric-field-dependent variations: the pristine microwire exhibited uniform topography and near-field amplitude. Under an applied bias (0.5 V μm^{-1} for 20 min), the near-field amplitude decreased from the positive to the negative electrode, indicating enhanced carrier accumulation near the positive contact. Corresponding phase images showed a locally increased refractive index near the negative electrode due to reduced absorption accompanying structural expansion. When a negative poling voltage is applied to the microwire, the opposite phenomenon can be observed. Furthermore, reversible lattice swelling and contraction correlated with light-induced halide redistribution were observed, demonstrating the intimate coupling between ionic movement and structural dynamics.

When integrated with complementary AFM-based electrical and optical techniques, AFM-IR and PTIR together constitute a comprehensive platform for probing local chemistry, phase behavior, and ion transport in perovskite-based optoelectronic systems. Ultimately, these methodologies offer critical insights into the structure–property–function relationships that underpin the performance and long-term stability of halide perovskites.

3.3 KPFM-based scattering-SNOM (s-SNOM) and surface photovoltage microscopy (SPVM)

When carefully optimized and integrated with complementary techniques such as AFM or KPFM, s-SNOM becomes a powerful tool for exploring nanoscale light–matter interactions. This approach enables spatially resolved analysis of absorption, emission, and plasmonic behavior in complex optoelectronic systems, including halide perovskites.

To investigate the interplay between local optical and electrical properties at GBs, correlative KPFM and broadband s-SNOM measurements were conducted simultaneously in a single-pass scan as shown in Fig. 16.[143] The topography (Fig. 16a) of $CH_3NH_3PbI_3$ polycrystalline films shows grain sizes of 200–500 nm. CPD maps revealed enhanced surface potential at GBs (Fig. 16b), indicative of downward band bending and electron accumulation. The corresponding s-SNOM amplitude image (Fig. 16c) showed increased infrared response at GBs, with line profiles (Fig. 16d) confirming superior spatial resolution of s-SNOM (~27 nm) compared to KPFM (~57 nm). Despite differences in resolution, these correlative measurements

Open Access Article. Published on 26 March 2026. Downloaded on 6/16/2026 7:27:17 AM.
This article is licensed under a Creative Commons Attribution-NonCommercial 3.0 Unported Licence.

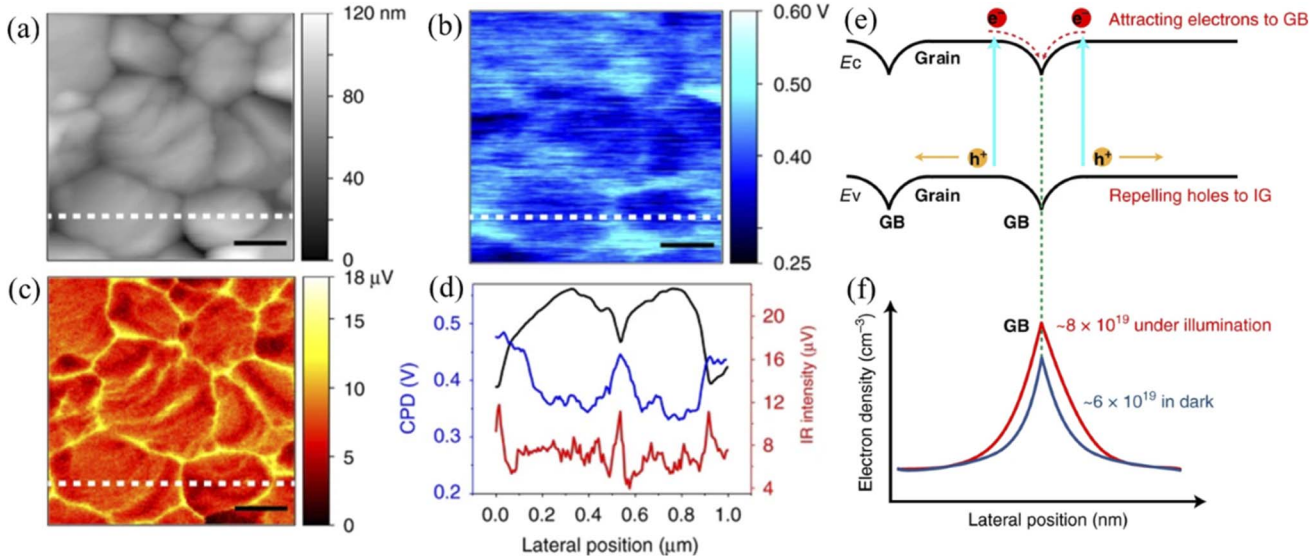

Fig. 16 (a) AFM topography, (b) KPFM and (c) infrared near-field images of $CH_3NH_3PbI_3$ polycrystalline films. The scale bar is 200 nm. (d) Line profiles of the topography, infrared near-field amplitude and CPD along the white dashed lines marked in (a–c). (e) Schematic illustration of the band alignment between grains and GBs. (f) Schematic illustration of electron density around the GB with and without additional light illumination. Reproduced from ref. 143 with permission from Springer Nature,[143] copyright 2021.

provide critical insights into GB-driven electronic behavior. The built-in potential at GBs promotes electron accumulation and hole exclusion, enhancing charge separation and reducing recombination, as shown in the band bending diagram in Fig. 16e. Furthermore, it induces local polarity inversion at the GBs, with estimated electron densities rising from $\sim 6 \times 10^{19}$ cm^{-3} in the dark to $\sim 8 \times 10^{19}$ cm^{-3} under illumination (Fig. 16f). These findings parallel similar phenomena observed in Cu(In,Ga)Se_2 solar cells and offer direct nanoscale evidence of space-charge-induced carrier redistribution in halide perovskites.[143]

The combination of KPFM and s-SNOM enables a comprehensive evaluation of the surface potential distribution of halide perovskites, as well as its variation under illumination, from both optical and electrical perspectives. Furthermore, another AFM-based technique for investigating the photoelectric effect on material surfaces is SPVM.[137,146] SPVM is a technique derived from KPFM, which enables nanoscale visualization of photoinduced electrical responses at semiconductor surfaces. Unlike traditional SPV measurements that lack spatial resolution, SPVM allows the correlation of local structural features with photophysical performance, providing a microscopic basis for understanding and improving macroscopic device behavior. In the field of halide perovskite solar cells, where spatial inhomogeneities critically influence charge dynamics and overall device performance, SPVM offers a powerful, non-destructive tool for probing local photovoltage variations with high spatial resolution. SPVM has proven particularly valuable in identifying defect-prone regions, interfacial discontinuities, and GB effects, which often act as carrier recombination centers or charge accumulation sites. In SPVM, the tip–sample junction is illuminated with a modulated light source during the KPFM measurement. This optical perturbation induces a local change in CPD due to photoexcited carrier generation and separation. The resulting CPD shift corresponds to the SPV, which reflects changes in band bending and local electric field distribution at the illuminated site. Therefore, SPVM effectively maps how photo-carriers accumulate, separate, and diffuse, offering direct insight into the nanoscale optoelectronic heterogeneity of the perovskite film. SPVM emerges as a critical technique in the development of high-efficiency perovskite optoelectronic devices, offering unique insights into the local dynamics of photo response, charge separation, and defect-induced recombination. As perovskite-based devices move toward commercial viability, the role of SPVM in bridging nanoscale characterization and device-level optimization will only grow in significance.

However, the time resolution of SPVM remains limited due to intrinsic feedback and detection delays in AFM systems. Standard KPFM-based SPVM requires a bias feedback loop to nullify the electrostatic force between the AFM tip and sample, resulting in a time resolution of ~1 ms (as demonstrated in measurements on Cu_2O photocatalyst particles).[137,146] Even with advanced feedback-free approaches, nanosecond resolution remains out of reach due to the inherently slow mechanical and electronic response of AFM systems.

4 Time-resolved surface and interface measurements for halide perovskites

While SPVM provides valuable static maps of photoinduced potential distributions, it yields only a time-averaged view of the charge dynamics under illumination. However, carrier generation, transport, trapping, and recombination in halide

© 2026 The Author(s). Published by the Royal Society of Chemistry

Open Access Article. Published on 26 March 2026. Downloaded on 6/16/2026 7:27:17 AM.
This article is licensed under a Creative Commons Attribution-NonCommercial 3.0 Unported Licence.

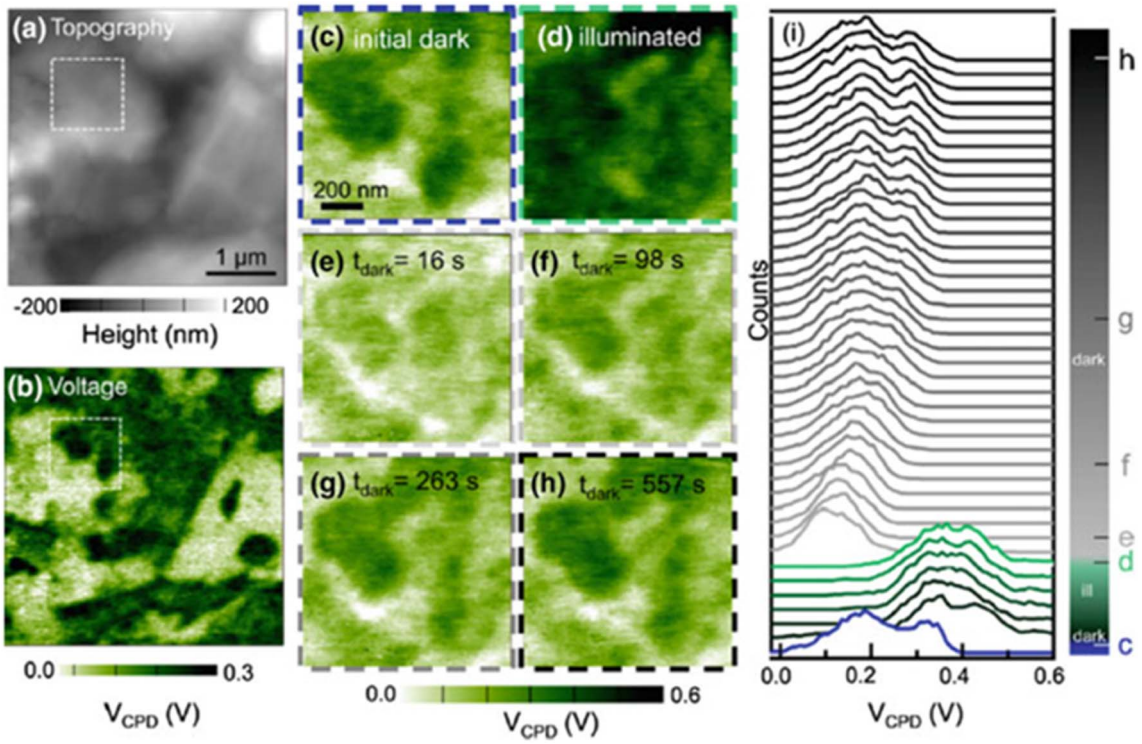

Fig. 17 Dynamics of halide perovskite solar cells at the nanoscale. (a) Topography and (b) KPFM measurements on the same area of the $MAPbI_3$ layer in the dark. A sequence of fast-KPFM measurements were acquired on the region highlighted by the white dashed square in (a and b): (c) dark-KPFM, (d) illuminated-KPFM with 500 nm laser light at 54 μW. (e–h) KPFM images after illumination was switched on, the time is mentioned in the images. (i) Histograms of CPD images taken over time, including measurements initially in the dark, under illumination, and after light switch off. Reproduced from ref. 118 with permission from the American Chemical Society,[118] copyright 2017.

perovskites occur across a wide range of timescales, from femtoseconds to seconds. Understanding these dynamic processes is crucial for elucidating charge separation and extraction mechanisms, which directly influence the performance of optoelectronic and catalytic devices. To bridge this gap, time-resolved KPFM (tr-KPFM) techniques have been developed to probe the temporal evolution of SPV signals at the nanoscale. These methods typically involve synchronizing modulated or pulsed laser illumination with lock-in detection, fast feedback loops, or even feedback-free readout schemes, allowing researchers to track transient carrier behavior with increasing temporal resolution. For instance, modulating the laser source and using a lock-in amplifier enables phase-sensitive detection of SPV transients, separating fast and slow components of the response.

4.1 Fast-Kelvin probe force microscopy (fast-KPFM)

A fast-KPFM with heterodyne detection scheme has emerged as a powerful variant of conventional KPFM, enabling real-time mapping of surface potential dynamics with improved temporal resolution. This advancement is particularly critical in the study of halide perovskite solar cells, where slow ionic movements can strongly influence the optoelectronic landscape and complicate the interpretation of conventional, static KPFM measurements. Garrett *et al.* employed fast-KPFM to study $CH_3NH_3PbI_3$ thin films on ITO/PEDOT:PSS substrates.[118] By capturing several surface potential maps per minute, fast-KPFM can observe temporal evolution of the surface potential under dark and illuminated conditions (Fig. 17). Notably, the imaging sequence highlighted that the changes in surface potential persist even after illumination is ceased, reflecting a non-negligible ionic contribution to the local electric landscape. While these dynamic surface potential shifts could superficially resemble SPV transients or local open-circuit voltage changes, they are dominated by ion migration or the redistribution of mobile ionic species such as I^-, MA^+, or Pb^{2+}, rather than by photo-carrier processes. Their results revealed a delayed and gradual relaxation of surface potential following illumination, with the system requiring several minutes to return to equilibrium.

However, disentangling the complex interplay between ionic motion, trapped charges, and photo-generated carriers remains a key challenge for future KPFM studies. For instance, while ion migration offers a plausible explanation for the long relaxation times, slow de-trapping of photo-excited carriers might also contribute to the observed potential transients. Moreover, the co-existence of permanent interfacial dipoles or defect-induced fixed charges can further complicate data interpretation. Overall, the application of fast-KPFM marks a significant step toward nanoscale time-resolved characterization of perovskite-based devices, providing unique insights into the electrochemical dynamics that influence device stability, hysteresis behavior,

Open Access Article. Published on 26 March 2026. Downloaded on 6/16/2026 7:27:17 AM.
This article is licensed under a Creative Commons Attribution-NonCommercial 3.0 Unported Licence.

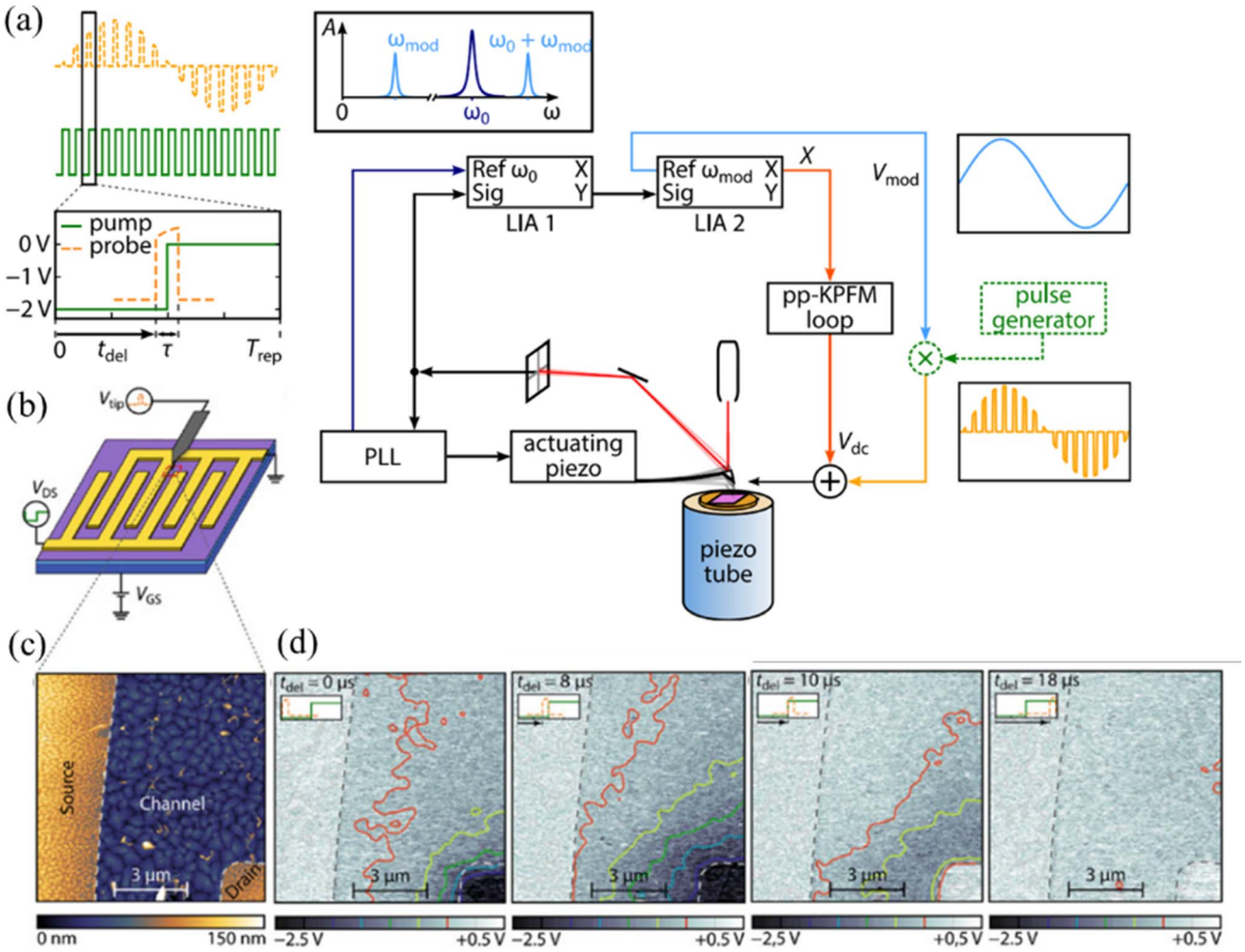

Fig. 18 (a) Schematic illustration of the measurement principle of a bias-modulated pp-KPFM. The pulse generator and lock-in amplifier are used on the basis of a conventional KPFM setup. The pump and probe pulses are shown with a green line and yellow line, respectively. (b) Schematic illustration of an organic field effect transistor (OFET) with interdigitated gold electrodes in a pp-KPFM configuration. The red dashed line illustrates the measured area for which the topography is shown in (c). (d) pp-KPFM images at specific time delays of the probe pulse with respect to pump pulse, which has a repetition frequency of 50 kHz (corresponding to a cycle time of 20 μs). The probe-to-pump pulse relationship is illustrated in the top left corner of each image. Isopotential lines are indicated by the colored solid lines which show the evolution of the CPD in the transistor channel. Reproduced from ref. 136 with permission from AIP Publishing,[136] copyright 2015.

and long-term performance. Continued development of high-speed and high-sensitivity KPFM techniques will be essential for uncovering the fundamental physics governing ionic–electronic coupling in emerging halide perovskites.

4.2 Pump-probe Kelvin probe force microscopy (pp-KPFM)

To address the inherent temporal limitations of tr-KPFM, pp-KPFM has been developed.[135,136,138–140,144,204] This technique decouples temporal resolution from cantilever dynamics, overcoming the bandwidth constraints of KPFM's feedback loop and cantilever response time, thereby enabling access to nanosecond-scale electrodynamic phenomena. In particular, pp-KPFM applies a time-dependent perturbation to probe transient charge dynamics in materials *via* an optical or electrical pulse. While it provides valuable insights into the coupling between local morphology and electronic behavior, its temporal resolution remains constrained by the mechanical bandwidth of the AFM system. Moreover, interpretation of transient CPD signals is often complicated by the coexistence of electrostatic and photoinduced contributions. Despite these challenges, pp-KPFM has become an essential tool for time-resolved nanoscale analysis of charge generation, trapping, and transport in emerging optoelectronic materials.

In bias-modulated pp-KPFM, a periodic bias pulse is applied to the sample or tip to mimic excitation conditions, and the time-dependent changes in CPD are measured with nanometer spatial resolution. This enables the investigation of key processes such as carrier injection, trapping/detrapping, and relaxation in semiconductors and dielectrics. In a typical pp-KPFM setup, a square-wave "pump" signal (green trace) is used to induce transient electrical excitation in the sample (Fig. 18a).[136] A "probe" pulse, consisting of a sinusoidal waveform with intermittent grounding intervals (yellow dashed

© 2026 The Author(s). Published by the Royal Society of Chemistry

Open Access Article. Published on 26 March 2026. Downloaded on 6/16/2026 7:27:17 AM.
This article is licensed under a Creative Commons Attribution-NonCommercial 3.0 Unported Licence.

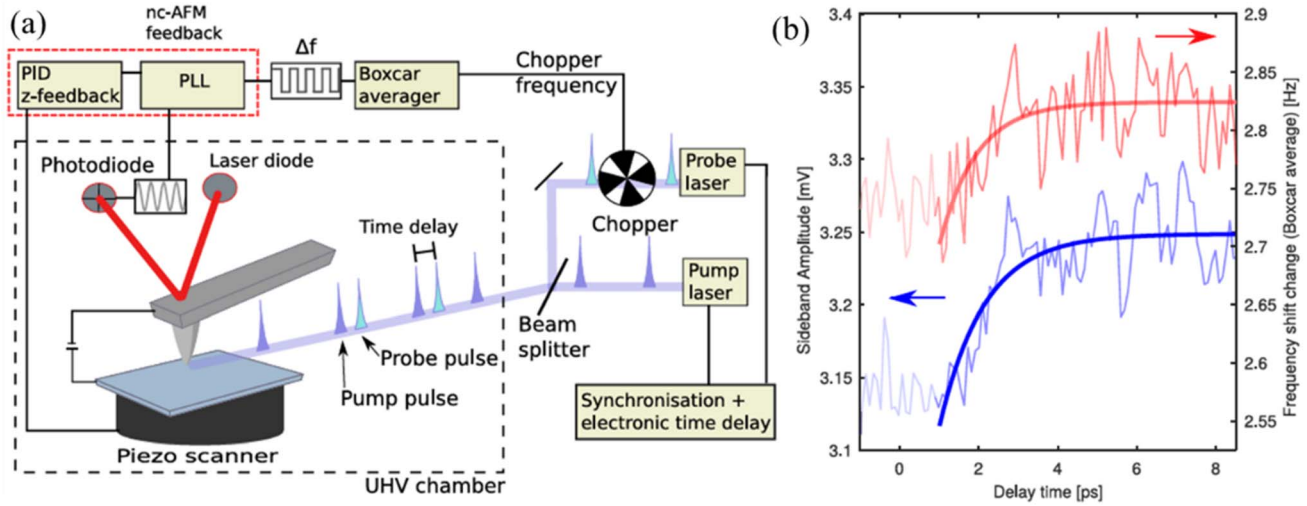

Fig. 19 (a) Schematic illustration of an optical pp-KPFM. A pump pulse train (blue) and a probe pulse train (green) are delayed with respect to each other. The probe pulse train is additionally modulated by a chopper. The final pulse train pattern comprises the delayed pulse trains with and without the probe beam. The sample and cantilever react to this pulse train resulting in a modulation of the frequency shift. (b) Photocarrier decay measured in LT-GaAs at constant height (1 nm tip lift) and 950 mV bias. A 780 nm pump laser and a 610 nm probe laser are utilized. Decay time traces obtained by direct sideband detection (blue) and boxcar averaging (red) are compared in the time domain. Reproduced from ref. 135 with permission from AIP Publishing,[135] copyright 2017.

trace), is applied to the tip with a controllable delay relative to the pump. By scanning the pump-probe delay, one reconstructs the time-resolved evolution of surface potential at each pixel. Detection is based on frequency mixing, where the electrostatically induced resonance shift (ω_0) of the cantilever is read at a sideband frequency ($\omega_0 + \omega_{mod}$) using a lock-in amplifier. A feedback voltage is then applied to nullify the signal, allowing precise tracking of transient CPD. The system's temporal resolution is governed by the duration of the probe pulse, which can be as short as 4 ns with current pulse generators. Unlike fast-KPFM, which provides continuous time evolution over the excitation period, pp-KPFM produces discrete CPD maps at specific delay times, enabling targeted investigation of dynamic processes at selected time slices. To address topography-induced crosstalk, a dual-loop feedback configuration has been implemented: a standard KPFM loop compensates for the time-averaged CPD, while a secondary pp-KPFM loop detects transient CPD changes, thereby improving the accuracy of dynamic measurements.

An illustrative example (Fig. 18b–d) demonstrates CPD mapping of a pentacene thin film under electrical excitation. Upon applying −2 V to the source electrode (delay = 0 μs), the surface potential decreases according to the charge-carrier distribution within the channel, with a pronounced drop near the drain electrode, indicating insufficient carrier density and space-charge-limited transport. At 8 μs after switching, the isopotential lines become more evenly distributed, suggesting additional charge carriers injected from the source electrode. At 10 μs, shortly after the drain electrode is grounded, the gold electrode has returned to zero potential, while the channel still contains excess charge carriers, resulting in a non-equilibrium potential distribution. It takes approximately another 8 μs for the channel to fully deplete these excess carriers before the cycle restarts.[136] Such measurements exemplify the potential of pp-KPFM to resolve fast electronic processes at the nanoscale with both high spatial and temporal precision.

An alternative implementation of pp-KPFM leverages pulsed laser excitation rather than electrical pumping, enabling ultrafast time-resolved surface potential mapping by probing photoinduced charge dynamics.[135] In this approach, both pump and probe pulses are delivered optically, typically using lasers of different wavelengths. This configuration allows non-contact and all-optical access to excited-state carrier behavior with high temporal precision. Such an optical pp-KPFM employs pulsed or modulated illumination as the pump source to excite photo-carriers in optoelectronic materials, particularly useful for probing the local photo response of halide perovskites, organic photovoltaics, and 2D semiconductors. By synchronizing the optical pulse with the KPFM feedback, one can map spatially resolved surface photovoltage dynamics and track how photoinduced carriers redistribute and decay over time. In an optical pp-KPFM setup (Fig. 19a), a pump laser pulse (*e.g.*, 780 nm) excites the sample, altering its surface potential due to photoexcited carrier generation and redistribution. A subsequent probe pulse (*e.g.*, 610 nm) interacts with the sample at a controlled delay time, allowing the system's transient evolution to be probed at different time intervals after excitation. The cantilever detects changes in electrostatic force during the probe pulse, which is further enhanced by using a mechanical chopper to modulate the probe beam and improve the signal-to-noise ratio *via* lock-in detection. This method is sensitive to the difference in electrostatic force experienced by the cantilever at different delay times. The time-dependent signal reflects the decay kinetics of the photoinduced surface potential. Notably, two detection strategies can be employed: sideband detection, using lock-in amplification tuned to the frequency modulation

Open Access Article. Published on 26 March 2026. Downloaded on 6/16/2026 7:27:17 AM. This article is licensed under a Creative Commons Attribution-NonCommercial 3.0 Unported Licence.

of the probe pulse, and boxcar averaging, which integrates the frequency shift over a defined time window for each delay.

Fig. 19b illustrates time-resolved optical pp-KPFM spectra collected on low-temperature-grown GaAs (LT-GaAs), a material known for its ultrashort carrier lifetimes. Measurements performed at a tip–sample distance of 1 nm and under a 950 mV bias show an exponential decay in the signal, with fitted time constants of 1.1 ± 0.4 ps (sideband detection) and 0.9 ± 0.6 ps (boxcar averaging). These values closely match known carrier lifetimes of LT-GaAs, validating the technique's sensitivity and accuracy. This optical pp-KPFM setup currently demonstrates the fastest experimentally achieved temporal resolution in KPFM-based surface potential imaging—on the order of $\sim$1 picosecond.[135] The temporal resolution limit is primarily governed by the thermal noise of the cantilever, which dictates the smallest distinguishable electrostatic force variation between two successive delay times.

In summary, pp-KPFM enables high-resolution snapshots of fast surface potential dynamics, making it an ideal tool for investigating ultrafast charge injection, trapping, and transport processes at the nanoscale. While it lacks the continuous temporal insight of tr-KPFM, its temporal precision and selective probing capabilities offer powerful complementarity in the broader suite of time-resolved surface potential measurement techniques. In addition, the optical pp-KPFM represents a powerful advancement in time-resolved scanning probe techniques, allowing researchers to directly observe picosecond-scale charge relaxation processes in semiconductors and photoactive materials. The method is especially suited for materials with ultrafast dynamics and opens new possibilities for nanoscale photophysics research.

5 Artifacts in scanning probe microscopy for halide perovskites

The microscopic structure of the probe apex in real experiments often deviates significantly from the idealized geometries assumed in theoretical models. During scanning, tip–sample interactions can modify the apex structure, alter the effective tip work function and introduce uncertainties in measured surface potentials. At the atomic scale, the chemical nature of the apex atom strongly affects tunneling currents and short-range force interactions, which in turn result in topographic contrast and spatial resolution in STM and AFM.[205,206] Multiple nanoscale protrusions can result in multi-tip effects, producing distorted images. To minimize these artifacts, tip conditioning, apex functionalization, and calibration against reference samples (*e.g.*, Highly Oriented Pyrolytic Graphite, HOPG) are commonly employed, particularly under ultrahigh vacuum conditions. Under ambient conditions, precise tip manipulation is more challenging, necessitating careful control of tip stability throughout measurements.

In KPFM and its time-resolved variants, the tip condition is critical because the measured CPD directly depends on the effective tip work function. Long-range electrostatic interactions, including stray capacitance from the cantilever body and tip cone, can distort the measured signal.[207,208] Techniques such as lift-mode amplitude-modulation KPFM, frequency-modulation KPFM with no-feedback acquisition, and constant-height scanning under UHV conditions can reduce these artifacts, minimize feedback-induced errors, and improve measurement fidelity.[209]

When KPFM is applied to semiconductors, additional artifacts arise from tip-induced band bending and surface trap states.[197] Close tip–sample proximity can create a local electric field that modifies the surface band structure, while traps at surfaces and GBs capture carriers, shifting the local Fermi level and producing CPD variations. Under illumination, photo-induced charging is another major source of artifacts: photogenerated carriers may become trapped at defects, GBs, or interfaces, creating local electrostatic potentials that evolve over time. These effects are particularly significant in time-resolved measurements, where both electronic carrier dynamics and ionic relaxation can contribute to the observed signals.

Halide perovskites introduce additional challenges due to their mixed ionic–electronic transport properties.[44] Mobile species, such as halide ions and organic cations, can migrate under probe-induced electric fields or illumination, leading to time-dependent variations in surface potential and local conductivity. Ionic accumulation at GBs or interfaces can produce long-lived electrostatic signals that may be misinterpreted as purely electronic features.

Therefore, careful experimental design is required when applying SPM to halide perovskites. Strategies such as minimizing tip bias, controlling illumination conditions, performing time-resolved measurements, and combining KPFM with complementary techniques can help disentangle ionic, electronic, and trap-related contributions to the measured signals. Understanding these potential artifacts is essential for correctly interpreting atomic morphology and nanoscale surface potential measurements in halide perovskites.

6 Conclusion and outlook

In summary, this review highlights the crucial role of SPM and its derivative techniques in advancing the understanding of halide perovskites. Through the complementary use of AFM, STM, and KPFM, the structural, optoelectronic, and ionic characteristics of halide perovskites can be explored at the atomic scale, providing valuable insights into their microscopic behavior under illumination and its impact on device performance. Furthermore, by integrating SPM with advanced optical measurement approaches, macroscopic optoelectronic phenomena can be resolved down to the nanoscale, enabling direct observation of illumination-induced changes in carrier dynamics and interfacial processes.

In particular, KPFM has proven to be a pivotal technique for probing surface work function and charge distribution, and when combined with electrical or optical pump-probe methods, it extends SPM's capability into the high spatial-temporal domain. Such progress allows for the direct visualization of transient carrier migration and dynamic interfacial phenomena that govern device operation. Overall, the convergence of SPM

 © 2026 The Author(s). Published by the Royal Society of Chemistry

Open Access Article. Published on 26 March 2026. Downloaded on 6/16/2026 7:27:17 AM.
This article is licensed under a Creative Commons Attribution-NonCommercial 3.0 Unported Licence.

and optical spectroscopies establishes a powerful experimental framework for unraveling the complex interplay between structure, charge, and functionality in perovskite optoelectronic systems, paving the way for the rational design of next-generation, high-performance, and stable halide-perovskite-based devices.

Looking forward, further improvements in spatial resolution will be essential for deepening our understanding of nanoscale heterogeneity in perovskite materials. Although atomic or sub-nanometer resolution has been achieved under ideal conditions, many measurements on operational devices are still limited by tip geometry, environmental instability, and long-range electrostatic interactions. Future developments in ultra-sharp conductive probes, low-noise detection electronics, and advanced feedback algorithms are expected to enhance the reliability and reproducibility of high-resolution imaging. In addition, combining SPM with functional mapping techniques, such as c-AFM, PL-AFM, and s-SNOM, will enable simultaneous acquisition of structural and optoelectronic information with improved lateral precision. Such progress is particularly important for resolving GBs, defects, ion accumulation regions, and buried interfaces, all of which critically influence charge transport, recombination pathways, and long-term stability. Achieving true atomic-scale resolution in realistic device architecture will provide unprecedented insight into defect physics and interfacial band alignment.

Equally important is the advancement of temporal resolution. Many key processes in halide perovskites, including carrier trapping, ion migration, phase segregation, and interfacial charge transfer, occur on timescales ranging from femtoseconds to milliseconds. Conventional SPM techniques are often limited by relatively slow scanning speeds and feedback response times, which constrain their ability to capture ultrafast or transient phenomena. The integration of high-speed AFM, pump-probe technology, and advanced data acquisition systems offers a promising route toward bridging this gap. By synchronizing optical excitation with fast electrical detection, it becomes possible to monitor dynamic surface potential variations and transient photocurrent responses in real time. The development of tr-KPFM and other ultrafast SPM modalities will further enable the study of carrier recombination kinetics, ionic redistribution under bias, and reversible or irreversible structural transformations under illumination. Enhancing temporal resolution is therefore crucial for correlating nanoscale observations with device-level performance metrics such as hysteresis, efficiency roll-off, and operational degradation.

Another critical direction for future research is the implementation of *in situ* and *operando* characterization. Halide perovskites are highly sensitive to environmental factors, including moisture, oxygen, temperature, electric field, and light. Consequently, *ex situ* measurements performed under ambient or vacuum conditions may not fully represent the material behavior during real device operation. Developing environmental SPM platforms capable of controlling atmosphere, humidity, temperature, and illumination will allow systematic investigation of degradation pathways and phase evolution. *In situ* biasing experiments can reveal ion redistribution, interfacial polarization, and defect activation under realistic working conditions. Furthermore, integrating SPM with encapsulated device architecture or microfabricated test platforms will facilitate *operando* measurements that directly correlate nanoscale structural and electronic changes with macroscopic performance. Such approaches are indispensable for clarifying the mechanisms underlying long-term instability and for guiding effective strategies to suppress ion migration, defect formation, and interfacial degradation.

Beyond individual improvements in spatial and temporal capabilities, the future of SPM in halide perovskite related research will likely involve multimodal and correlative methodologies. Combining SPM with electron microscopy, synchrotron-based spectroscopies, or ultrafast optical techniques can provide complementary information across different length and time scales. Machine learning-assisted data analysis may also play an increasingly important role in extracting subtle correlations from large, multidimensional datasets. Through these synergistic developments, SPM will evolve from a primarily imaging-based technique into a comprehensive nanoscale diagnostic platform.

Continuous innovation in spatial resolution, temporal resolution, and *in situ operando* methodologies will significantly enhance the power of SPM techniques in the research of halide perovskites. These advances will enable a more thorough understanding of dynamic processes, defect physics, and interfacial phenomena that ultimately dictate device efficiency and stability. By bridging the gap between nanoscale mechanisms and macroscopic functionality, next-generation SPM approaches will remain at the forefront of fundamental studies and technological optimization of halide-perovskite-based optoelectronic systems.

Author contributions

Conceptualization, Z. Q., S. X.; writing – original draft preparation, Z. Q., J. C., and S. X.; writing – review and editing, S. X., Z. Q., and B. X.; supervision, S. X.; funding acquisition, S. X. All authors have read and agreed to the published version of the manuscript.

Conflicts of interest

The authors declare no competing financial interests.

Data availability

No primary research results, software or code have been included, and no new data were generated or analyzed as part of this review.

Supplementary information (SI): list of symbols and abbreviations. See DOI: https://doi.org/10.1039/d6el00030d.

Acknowledgements

The authors acknowledge the support from the National Key Research and Development Program of China

Open Access Article. Published on 26 March 2026. Downloaded on 6/16/2026 7:27:17 AM. This article is licensed under a Creative Commons Attribution-NonCommercial 3.0 Unported Licence.

(2024YFE0217100), the National Natural Science Foundation of China (21905006), the Shenzhen Science and Technology Program (SGDX20230116093205009), Guangdong Provincial Higher Education Special Innovation Program (2025KTSCX117) and the Natural Science Foundation of Top Talent of SZTU (GDRC202343).

References

1 C. C. Stoumpos and M. G. Kanatzidis, *Acc. Chem. Res.*, 2015, **48**, 2791–2802.
2 M. A. Green, A. Ho-Baillie and H. J. Snaith, *Nat. Photonics*, 2014, **8**, 506–514.
3 C. S. Ponseca, T. J. Savenije, M. Abdellah, K. Zheng, A. Yartsev, T. Pascher, T. Harlang, P. Chabera, T. Pullerits, A. Stepanov, J.-P. Wolf and V. Sundström, *J. Am. Chem. Soc.*, 2014, **136**, 5189–5192.
4 Q. Dong, Y. Fang, Y. Shao, P. Mulligan, J. Qiu, L. Cao and J. Huang, *Science*, 2015, **347**, 967–970.
5 X. Li, S. Gao, X. Wu, Q. Liu, L. Zhu, C. Wang, Y. Wang, Z. Liu, W. Chen, X. Li, P. Xiao, Q. Huang, T. Chen, Z. Li, X. Gao, Z. Xiao, Y. Lu, X. Zeng, S. Xiao, Z. Zhu and S. Yang, *Joule*, 2024, **8**, 3169–3185.
6 B. Li, D. Gao, C. Zhang, Z. Yu, M. Stolterfoht, Y. H. Lin, M. Lenz, H. J. Snaith and Z. Zhu, *Nat. Rev. Mater.*, 2025, **11**, 10–25.
7 J. Han, K. Park, S. Tan, Y. Vaynzof, J. Xue, E. W.-G. Diau, M. G. Bawendi, J.-W. Lee and I. Jeon, *Nat. Rev. Methods Primers*, 2025, **5**, 3.
8 Z. Yang, Q. Zhang, Y. Liu, B. Liu, Z. Zheng, G. Niu and L. Xu, *Adv. Electron. Mater.*, 2026, e00667.
9 I. Mora-Seró, *Joule*, 2018, **2**, 585–587.
10 J.-W. Lee, S. Tan, S. Il Seok, Y. Yang and N.-G. Park, *Science*, 2022, **375**, eabj1186.
11 Y. Ahmed, X. Qi, P. Moazzezi and M. I. Saidaminov, *ACS Energy Lett.*, 2026, **11**, 79–89.
12 B. Zhang, C. Hao, S. Zhang, B. Xue, X. Xie, S. Zeng, B. Yang, F. Xu, H. Li, X. Zhang, Z. Qu, K.-H. Ye, G. Niu, W. C. H. Choy, K. Fan, K. S. Wong, L. Yan, X. Wang, S. Xiao and C. Zhou, *Nano-Micro Lett.*, 2026, **18**, 89.
13 S. Zeng, B. Xue, B. Zhang, B. Yang, X. Xie, C. Hao, X. Wang, L. Qian, A. A. Petrov, G. Niu, W. C. H. Choy and S. Xiao, *Chem. Eng. J.*, 2025, **514**, 163060.
14 B. Yang, X. Xie, S. Zeng, B. Xue, S. Xiao and L. Qian, *Phys. Scr.*, 2024, **99**, 025995.
15 C. Xiao, Q. Zhao, C.-S. Jiang, Y. Sun, M. M. Al-Jassim, S. U. Nanayakkara and J. M. Luther, *Nano Energy*, 2020, **78**, 105319.
16 T. Baikie, Y. Fang, J. M. Kadro, M. Schreyer, F. Wei, S. G. Mhaisalkar, M. Graetzel and T. J. White, *J. Mater. Chem. A*, 2013, **1**, 5628.
17 H. S. Kim, C. R. Lee, J. H. Im, K. B. Lee, T. Moehl, A. Marchioro, S. J. Moon, R. Humphry-Baker, J. H. Yum, J. E. Moser, M. Grätzel and N. G. Park, *Sci. Rep.*, 2012, **2**, 591.
18 K. Galkowski, A. Mitioglu, A. Miyata, P. Plochocka, O. Portugall, G. E. Eperon, J. T.-W. Wang, T. Stergiopoulos, S. D. Stranks, H. J. Snaith and R. J. Nicholas, *Energy Environ. Sci.*, 2016, **9**, 962–970.
19 A. Miyata, A. Mitioglu, P. Plochocka, O. Portugall, J. T. W. Wang, S. D. Stranks, H. J. Snaith and R. J. Nicholas, *Nat. Phys.*, 2015, **11**, 582–587.
20 S. D. Stranks, G. E. Eperon, G. Grancini, C. Menelaou, M. J. P. Alcocer, T. Leijtens, L. M. Herz, A. Petrozza and H. J. Snaith, *Science*, 2013, **342**, 341–344.
21 Y. Tian, Y. An and B. Zhang, *Adv. Energy Mater.*, 2023, **13**, 2302119.
22 S. Xiao, W. Qian and S. Yang, *Adv. Energy Mater.*, 2023, **13**, 2201472.
23 National Renewable Energy Laboratory, Best Research-Cell Efficiency, https://www.nlr.gov/pv/cell-efficiency, accessed 13 February 2026.
24 A. Al-Ashouri, E. Köhnen, B. Li, A. Magomedov, H. Hempel, P. Caprioglio, J. A. Márquez, A. B. Morales Vilches, E. Kasparavicius, J. A. Smith, N. Phung, D. Menzel, M. Grischek, L. Kegelmann, D. Skroblin, C. Gollwitzer, T. Malinauskas, M. Jošt, G. Matič, B. Rech, R. Schlatmann, M. Topič, L. Korte, A. Abate, B. Stannowski, D. Neher, M. Stolterfoht, T. Unold, V. Getautis and S. Albrecht, *Science*, 2020, **370**, 1300–1309.
25 S. S. Shin, E. J. Yeom, W. S. Yang, S. Hur, M. G. Kim, J. Im, J. Seo, J. H. Noh and S. Il Seok, *Science*, 2017, **356**, 167–171.
26 Z. Liang, Y. Zhang, H. Xu, W. Chen, B. Liu, J. Zhang, H. Zhang, Z. Wang, D. H. Kang, J. Zeng, X. Gao, Q. Wang, H. Hu, H. Zhou, X. Cai, X. Tian, P. Reiss, B. Xu, T. Kirchartz, Z. Xiao, S. Dai, N. G. Park, J. Ye and X. Pan, *Nature*, 2023, **624**, 557–563.
27 M. A. Green, E. D. Dunlop, M. Yoshita, N. Kopidakis, K. Bothe, G. Siefer and X. Hao, *Prog. Photovoltaics*, 2023, **31**, 651–663.
28 Y. Wang, W. Li, X. Wu, G. Meng, Q. Liu, W. Zhao, B. Li, F. Vanin, H. Li, Y. Shi, S. Wang, Z. Tian, L. Zhang, J. Zhang, Z. Zhu and Y. Shi, *Nat. Energy*, 2025, **11**, 47–57.
29 W. Li, J. Zhang, L. Zeng, W. Wang, Z. Fang, X. Liu, Z. Ma, Y. Zhang, H. Yan, C. Shen, Z. Xue, J. Zhu, Q. Luo, C. Liu, R. Jiang, T. Bu, W. Tang, J. Li, S. Wang, J. Gong and X. Xiao, *Nat. Commun.*, 2025, **17**, 711.
30 D. Gao, B. Li, X. Sun, Q. Liu, C. Zhang, L. Qian, Z. Yu, X. Li, X. Wu, B. Liu, N. Wang, F. Vanin, X. Xia, J. Gong, N. Li, X. C. Zeng, Z. Li and Z. Zhu, *Nat. Photonics*, 2025, **19**, 1070–1077.
31 C. Besleaga, L. E. Abramiuc, V. Stancu, A. G. Tomulescu, M. Sima, L. Trinca, N. Plugaru, L. Pintilie, G. A. Nemnes, M. Iliescu, H. G. Svavarsson, A. Manolescu and I. Pintilie, *J. Phys. Chem. Lett.*, 2016, **7**, 5168–5175.
32 I. Ghani, S. Tingshu, S. Ahmed, Z. Hongbin, Z. Zirun, Y. Zhang, P. You, I. Muhammad, T. Zeguo and D. Khan, *Adv. Sci.*, 2025, e18676.
33 L. Wang, N. Wang, N. Kalasariya, X. Sun, X. Wu, Z. Yu, B. Li, Y. Qiao, K. Long Wong, A. F. Castro Mendez, O. Karalis, C. Zhang, D. Gao, H. Hempel, J. Wang, J. Yang, H. Jin, Y. Bai, X. Zhang, M. Xu, T. Unold, F. Lang, J. Yin, M. Stolterfoht and Z. Zhu, *Joule*, 2025, **9**, 102174.

 © 2026 The Author(s). Published by the Royal Society of Chemistry

Open Access Article. Published on 26 March 2026. Downloaded on 6/16/2026 7:27:17 AM. This article is licensed under a Creative Commons Attribution-NonCommercial 3.0 Unported Licence.

34 Y. Lu, Y.-K. Jung, M. Dubajic, X. Li, S. Maqbool, Q. Gu, X. Bai, Y. Boeije, X. W. Chua, A. J. Mirabelli, T. Kang, L. Sonneveld, Y. Zhang, T. A. Selby, C. Mamak, K. Tang, Z. Yu, T. Liu, M. Anaya, S. Barlow, S. R. Marder, B. Ehrler, C. Ducati, R. H. Friend and S. D. Stranks, *Science*, 2025, **390**, 716–721.
35 Y. Liu, Y. Zhang, X. Zhu, Z. Yang, W. Ke, J. Feng, X. Ren, K. Zhao, M. Liu, M. G. Kanatzidis and S. Frank Liu, *Sci. Adv.*, 2021, **7**, eabc8844.
36 T. Li, X. Luo, P. Wang, Z. Li, Y. Li, J. Huang, Z. Jin, Y. Yang, B. Li, W. Zhang, S. Lin, Y. Rui, H. Wang, Q. Zhang, Y. Zhan, B. Xu, J. Liang and Y. Qi, *Nature*, 2025, **648**, 84–90.
37 Y. Wang, T. Wu, J. Barbaud, W. Kong, D. Cui, H. Chen, X. Yang and L. Han, *Science*, 2019, **365**, 687–691.
38 Y. Cheng, X. Liu, Z. Guan, M. Li, Z. Zeng, H. Li, S. Tsang, A. G. Aberle and F. Lin, *Adv. Mater.*, 2021, **33**, 2006170.
39 Y. Yuan and J. Huang, *Acc. Chem. Res.*, 2016, **49**, 286–293.
40 J.-F. Wang, D.-X. Lin and Y.-B. Yuan, *Acta Phys. Sin.*, 2019, **68**, 158801.
41 X. Ren, L. Zhang, Y. Yuan and L. Ding, *J. Semicond.*, 2021, **42**, 010201.
42 W. Zhou, Y. Zhao, X. Zhou, R. Fu, Q. Li, Y. Zhao, K. Liu, D. Yu and Q. Zhao, *J. Phys. Chem. Lett.*, 2017, **8**, 4122–4128.
43 W. Yu, X. Sun, M. Xiao, T. Hou, X. Liu, B. Zheng, H. Yu, M. Zhang, Y. Huang and X. Hao, *Nano Res.*, 2022, **15**, 85–103.
44 J. Thiesbrummel, J. V. Milić, C. Deibel, E. C. Garnett, S. Tao, T. Kirchartz, A. Guerrero, P. Cameron, W. Tress, M. Saiful Islam and B. Ehrler, *Nat. Rev. Chem.*, 2026, **10**, 179–195.
45 D. Gao, B. Li, Q. Liu, C. Zhang, Z. Yu, S. Li, J. Gong, L. Qian, F. Vanin, K. Schutt, M. A. Davis, A. F. Palmstrom, S. P. Harvey, N. J. Long, J. M. Luther, X. C. Zeng and Z. Zhu, *Science*, 2024, **386**, 187–192.
46 N. Adhikari, A. Dubey, D. Khatiwada, A. F. Mitul, Q. Wang, S. Venkatesan, A. Iefanova, J. Zai, X. Qian, M. Kumar and Q. Qiao, *ACS Appl. Mater. Interfaces*, 2015, **7**, 26445–26454.
47 R. Szostak, J. C. Silva, S.-H. Turren-Cruz, M. M. Soares, R. O. Freitas, A. Hagfeldt, H. C. N. Tolentino and A. F. Nogueira, *Sci. Adv.*, 2019, **5**, eaaw6619.
48 Q. Chen, H. Zhou, T.-B. Song, S. Luo, Z. Hong, H.-S. Duan, L. Dou, Y. Liu and Y. Yang, *Nano Lett.*, 2014, **14**, 4158–4163.
49 H. Zai, Y. Ma, Q. Chen and H. Zhou, *J. Energy Chem.*, 2021, **63**, 528–549.
50 M. Li, P. Wu, J. Liu, X. Lang, Y. Shi, X. Liu, H. Tian, Y. Jiang, Y. Gou, Y. Zhang, Z. Yang, J. Ye, Y. Zhai, F. Zhang and C. Xiao, *Newton*, 2025, 100367.
51 Y. Zhao, W. Zhou, H. Tan, R. Fu, Q. Li, F. Lin, D. Yu, G. Walters, E. H. Sargent and Q. Zhao, *J. Phys. Chem. C*, 2017, **121**, 14517–14523.
52 M. A. Green, E. D. Dunlop, M. Yoshita, N. Kopidakis, K. Bothe, G. Siefer, D. Hinken, M. Rauer, J. Hohl-Ebinger and X. Hao, *Prog. Photovoltaics*, 2024, **32**, 425–441.
53 A. Ghosh, D. K. Chaudhary, A. Mandal, S. Prodhan, K. K. Chauhan, S. Vihari, G. Gupta, P. K. Datta and S. Bhattacharyya, *J. Phys. Chem. Lett.*, 2020, **11**, 591–600.
54 G. E. Eperon, D. Moerman and D. S. Ginger, *ACS Nano*, 2016, **10**, 10258–10266.
55 A. Morteza Najarian, M. Vafaie, B. Chen, F. P. García de Arquer and E. H. Sargent, *Nat. Rev. Phys.*, 2024, **6**, 219–230.
56 H. J. Snaith, A. Abate, J. M. Ball, G. E. Eperon, T. Leijtens, N. K. Noel, S. D. Stranks, J. T.-W. Wang, K. Wojciechowski and W. Zhang, *J. Phys. Chem. Lett.*, 2014, **5**, 1511–1515.
57 E. L. Unger, E. T. Hoke, C. D. Bailie, W. H. Nguyen, A. R. Bowring, T. Heumüller, M. G. Christoforo and M. D. McGehee, *Energy Environ. Sci.*, 2014, **7**, 3690–3698.
58 R. Wiesendanger, *Scanning Probe Microscopy and Spectroscopy*, Cambridge University Press, 1994.
59 S. Morita and Y. Sugawara, *Noncontact Atomic Force Microscopy*, Springer, 2002.
60 S. Sadewasser and T. Glatzel, *Kelvin Probe Force Microscopy*, Springer, 2018.
61 G. Binnig, C. F. Quate and Ch. Gerber, *Phys. Rev. Lett.*, 1986, **56**, 930–933.
62 M. Lanza, *Conductive Atomic Force Microscopy: Applications in Nanomaterials*, Wiley, 2017.
63 J. Hieulle, C. Stecker, R. Ohmann, L. K. Ono and Y. Qi, *Small Methods*, 2018, **2**, 1700295.
64 P. Pansa-Ngat, S. Kamnoedmanee, N. Semapet, K. Sinthiptharakoon, C. Suwanchawalit, S. Burimart, C. Seriwattanachai, K. K. Shin Thant and P. Kanjanaboos, *ACS Appl. Energy Mater.*, 2024, **7**, 3234–3244.
65 G. Binnig, H. Rohrer, Ch. Gerber and E. Weibel, *Phys. Rev. Lett.*, 1982, **49**, 57–61.
66 G. Binnig, H. Rohrer, Ch. Gerber and E. Weibel, *Phys. Rev. Lett.*, 1983, **50**, 120–123.
67 M.-C. Shih, S.-S. Li, C.-H. Hsieh, Y.-C. Wang, H.-D. Yang, Y.-P. Chiu, C.-S. Chang and C.-W. Chen, *Nano Lett.*, 2017, **17**, 1154–1160.
68 L. She, M. Liu, X. Li, Z. Cai and D. Zhong, *Surf. Sci.*, 2017, **656**, 17–23.
69 B. Murali, S. Dey, A. L. Abdelhady, W. Peng, E. Alarousu, A. R. Kirmani, N. Cho, S. P. Sarmah, M. R. Parida, M. I. Saidaminov, A. A. Zhumekenov, J. Sun, M. S. Alias, E. Yengel, B. S. Ooi, A. Amassian, O. M. Bakr and O. F. Mohammed, *ACS Energy Lett.*, 2016, **1**, 1119–1126.
70 Y. Liu, K. Palotas, X. Yuan, T. Hou, H. Lin, Y. Li and S.-T. Lee, *ACS Nano*, 2017, **11**, 2060–2065.
71 A. Poglitsch and D. Weber, *J. Chem. Phys.*, 1987, **87**, 6373–6378.
72 L. She, M. Liu and D. Zhong, *ACS Nano*, 2016, **10**, 1126–1131.
73 J. Qi, W. Zhang and R. Cao, *Adv. Energy Mater.*, 2018, **8**, 1701620.
74 F. J. Giessibl, *Science*, 1995, **267**, 68–71.
75 F. J. Giessibl, *Rev. Mod. Phys.*, 2003, **75**, 949–983.
76 F. Cai, L. Yang, Y. Yan, J. Zhang, F. Qin, D. Liu, Y.-B. Cheng, Y. Zhou and T. Wang, *J. Mater. Chem. A*, 2017, **5**, 9402–9411.
77 S. Ahn, W. Jang, J. Hyeok Park and D. Hwan Wang, *RSC Adv.*, 2016, **6**, 51513–51519.
78 M. Long, T. Zhang, W. Xu, X. Zeng, F. Xie, Q. Li, Z. Chen, F. Zhou, K. S. Wong, K. Yan and J. Xu, *Adv. Energy Mater.*, 2017, **7**, 1601882.
79 J. Song, L. Liu, X.-F. Wang, G. Chen, W. Tian and T. Miyasaka, *J. Mater. Chem. A*, 2017, **5**, 13439–13447.

Open Access Article. Published on 26 March 2026. Downloaded on 6/16/2026 7:27:17 AM. This article is licensed under a Creative Commons Attribution-NonCommercial 3.0 Unported Licence.

80 X. Xu, Z. Zhang, T. Liu, P. Zhu, Z. Zhang and G. Xing, *J. Mater. Chem. A*, 2025, **13**, 12097–12103.
81 J. J. Li, J. Y. Ma, J. S. Hu, D. Wang and L. J. Wan, *ACS Appl. Mater. Interfaces*, 2016, **8**, 26002–26007.
82 N. Zhou, Y. Shen, Y. Zhang, Z. Xu, G. Zheng, L. Li, Q. Chen and H. Zhou, *Small*, 2017, **13**, 1700484.
83 C. Wang, C. Zhang, S. Tong, J. Shen, C. Wang, Y. Li, S. Xiao, J. He, J. Zhang, Y. Gao and J. Yang, *J. Phys. Chem. C*, 2017, **121**, 6575–6580.
84 M. Sun, F. Zhang, H. Liu, X. Li, Y. Xiao and S. Wang, *J. Mater. Chem. A*, 2017, **5**, 13448–13456.
85 P. Zhao, W. Yin, M. Kim, M. Han, Y. J. Song, T. K. Ahn and H. S. Jung, *J. Mater. Chem. A*, 2017, **5**, 7905–7911.
86 H. Yuan, E. Debroye, K. Janssen, H. Naiki, C. Steuwe, G. Lu, M. Moris, E. Orgiu, H. Uji-i, F. De Schryver, P. Samorì, J. Hofkens and M. Roeffaers, *J. Phys. Chem. Lett.*, 2016, **7**, 561–566.
87 K. Sun, J. Chang, F. H. Isikgor, P. Li and J. Ouyang, *Nanoscale*, 2015, **7**, 896–900.
88 M. Remeika, S. R. Raga, S. Zhang and Y. Qi, *J. Mater. Chem. A*, 2017, **5**, 5709–5718.
89 M. Ralaiarisoa, Y. Busby, J. Frisch, I. Salzmann, J.-J. Pireaux and N. Koch, *Phys. Chem. Chem. Phys.*, 2017, **19**, 828–836.
90 J. Qing, H.-T. Chandran, Y.-H. Cheng, X.-K. Liu, H.-W. Li, S.-W. Tsang, M.-F. Lo and C.-S. Lee, *ACS Appl. Mater. Interfaces*, 2015, **7**, 23110–23116.
91 W. Nie, H. Tsai, R. Asadpour, J.-C. Blancon, A. J. Neukirch, G. Gupta, J. J. Crochet, M. Chhowalla, S. Tretiak, M. A. Alam, H.-L. Wang and A. D. Mohite, *Science*, 2015, **347**, 522–525.
92 X. Li, D. Bi, C. Yi, J.-D. Décoppet, J. Luo, S. M. Zakeeruddin, A. Hagfeldt and M. Grätzel, *Science*, 2016, **353**, 58–62.
93 M. Kim, G.-H. Kim, K. S. Oh, Y. Jo, H. Yoon, K.-H. Kim, H. Lee, J. Y. Kim and D. S. Kim, *ACS Nano*, 2017, **11**, 6057–6064.
94 L.-L. Jiang, S. Cong, Y.-H. Lou, Q.-H. Yi, J.-T. Zhu, H. Ma and G.-F. Zou, *J. Mater. Chem. A*, 2016, **4**, 217–222.
95 L.-L. Gao, L.-S. Liang, X.-X. Song, B. Ding, G.-J. Yang, B. Fan, C.-X. Li and C.-J. Li, *J. Mater. Chem. A*, 2016, **4**, 3704–3710.
96 G. Gao, Q. Xi, H. Zhou, Y. Zhao, C. Wu, L. Wang, P. Guo and J. Xu, *Nanoscale*, 2017, **9**, 12032–12038.
97 L. A. Frolova, D. V. Anokhin, A. A. Piryazev, S. Yu. Luchkin, N. N. Dremova, K. J. Stevenson and P. A. Troshin, *J. Phys. Chem. Lett.*, 2017, **8**, 67–72.
98 B. Ding, Y. Li, S.-Y. Huang, Q.-Q. Chu, C.-X. Li, C.-J. Li and G.-J. Yang, *J. Mater. Chem. A*, 2017, **5**, 6840–6848.
99 C. Li, J. Liu, H. Li, K. Wu, J. Wang and Q. Yang, *Nat. Commun.*, 2022, **13**, 2357.
100 Z. Zhao, X. Chen, H. Wu, X. Wu and G. Cao, *Adv. Funct. Mater.*, 2016, **26**, 3048–3058.
101 B. Lee, S. Lee, D. Cho, J. Kim, T. Hwang, K. H. Kim, S. Hong, T. Moon and B. Park, *ACS Appl. Mater. Interfaces*, 2016, **8**, 30985–30991.
102 B. El Cohen, S. Aharon, A. Dymshits and L. Etgar, *J. Phys. Chem. C*, 2015, **120**, 142–147.
103 J. J. Li, J. Y. Ma, Q. Q. Ge, J. S. Hu, D. Wang and L. J. Wan, *ACS Appl. Mater. Interfaces*, 2015, **7**, 28518–28523.
104 J. S. Yun, A. Ho-Baillie, S. Huang, S. H. Woo, Y. Heo, J. Seidel, F. Huang, Y.-B. Cheng and M. A. Green, *J. Phys. Chem. Lett.*, 2015, **6**, 875–880.
105 S. Y. Leblebici, L. Leppert, Y. Li, S. E. Reyes-Lillo, S. Wickenburg, E. Wong, J. Lee, M. Melli, D. Ziegler, D. K. Angell, D. F. Ogletree, P. D. Ashby, F. M. Toma, J. B. Neaton, I. D. Sharp and A. Weber-Bargioni, *Nat. Energy*, 2016, **1**, 16093.
106 Y. Kutes, Y. Zhou, J. L. Bosse, J. Steffes, N. P. Padture and B. D. Huey, *Nano Lett.*, 2016, **16**, 3434–3441.
107 H. Si, S. Zhang, S. Ma, Z. Xiong, A. Kausar, Q. Liao, Z. Zhang, A. Sattar, Z. Kang and Y. Zhang, *Adv. Energy Mater.*, 2020, **10**, 1903922.
108 J. S. Yun, J. Seidel, J. Kim, A. M. Soufiani, S. Huang, J. Lau, N. J. Jeon, S. Il Seok, M. A. Green and A. Ho-Baillie, *Adv. Energy Mater.*, 2016, **6**, 1600330.
109 A. Dymshits, A. Henning, G. Segev, Y. Rosenwaks and L. Etgar, *Sci. Rep.*, 2015, **5**, 8704.
110 Y. Fu, X. Zhu, L. Huang, X. Zhang, F. Zhang and W. Zhu, *Appl. Catal., B*, 2018, **239**, 46–51.
111 Y. Zhong, W. Dong, S. Ren and L. Li, *Adv. Mater.*, 2024, **36**, e2308251.
112 E. J. Spadafora, M. Linares, W. Z. Nisa Yahya, F. Lincker, R. Demadrille and B. Grevin, *Appl. Phys. Lett.*, 2011, **99**, 233102.
113 M. Li, X. Yan, Z. Kang, X. Liao, Y. Li, X. Zheng, P. Lin, J. Meng and Y. Zhang, *ACS Appl. Mater. Interfaces*, 2017, **9**, 7224–7231.
114 Y. C. Kim, N. J. Jeon, J. H. Noh, W. S. Yang, J. Seo, J. S. Yun, A. Ho-Baillie, S. Huang, M. A. Green, J. Seidel, T. K. Ahn and S. Il Seok, *Adv. Energy Mater.*, 2016, **6**, 1502104.
115 W. Melitz, J. Shen, A. C. Kummel and S. Lee, *Surf. Sci. Rep.*, 2011, **66**, 1–27.
116 B. Yang, C. C. Brown, J. Huang, L. Collins, X. Sang, R. R. Unocic, S. Jesse, S. V. Kalinin, A. Belianinov, J. Jakowski, D. B. Geohegan, B. G. Sumpter, K. Xiao and O. S. Ovchinnikova, *Adv. Funct. Mater.*, 2017, **27**, 1700749.
117 M. Nonnenmacher, M. P. O'Boyle and H. K. Wickramasinghe, *Appl. Phys. Lett.*, 1991, **58**, 2921–2923.
118 J. L. Garrett, E. M. Tennyson, M. Hu, J. Huang, J. N. Munday and M. S. Leite, *Nano Lett.*, 2017, **17**, 2554–2560.
119 Q. Chen, H. Zhou, Y. Fang, A. Z. Stieg, T.-B. Song, H.-H. Wang, X. Xu, Y. Liu, S. Lu, J. You, P. Sun, J. McKay, M. S. Goorsky and Y. Yang, *Nat. Commun.*, 2015, **6**, 7269.
120 V. W. Bergmann, S. A. L. Weber, F. Javier Ramos, M. K. Nazeeruddin, M. Grätzel, D. Li, A. L. Domanski, I. Lieberwirth, S. Ahmad and R. Berger, *Nat. Commun.*, 2014, **5**, 5001.
121 V. W. Bergmann, Y. Guo, H. Tanaka, I. M. Hermes, D. Li, A. Klasen, S. A. Bretschneider, E. Nakamura, R. Berger and S. A. L. Weber, *ACS Appl. Mater. Interfaces*, 2016, **8**, 19402–19409.
122 X. Tang, M. Van Den Berg, E. Gu, A. Horneber, G. J. Matt, A. Osvet, A. J. Meixner, D. Zhang and C. J. Brabec, *Nano Lett.*, 2018, **18**, 2172–2178.

 © 2026 The Author(s). Published by the Royal Society of Chemistry

Open Access Article. Published on 26 March 2026. Downloaded on 6/16/2026 7:27:17 AM. This article is licensed under a Creative Commons Attribution-NonCommercial 3.0 Unported Licence.

123 Y. Gim, H. K. Park, G. Lim, J. Kim, Y. S. Kim and W. Jo, *Nano Converg.*, 2026, **13**, 8.
124 C. Yang, P. Du, Z. Dai, H. Li, X. Yang and Q. Chen, *ACS Appl. Mater. Interfaces*, 2019, **11**, 14044–14050.
125 D. S. Jakob, H. Wang, G. Zeng, D. E. Otzen, Y. Yan and X. G. Xu, *Angew. Chem., Int. Ed.*, 2020, **59**, 16083–16090.
126 H. Chen, A. Maxwell, C. Li, S. Teale, B. Chen, T. Zhu, E. Ugur, G. Harrison, L. Grater, J. Wang, Z. Wang, L. Zeng, S. M. Park, L. Chen, P. Serles, R. A. Awni, B. Subedi, X. Zheng, C. Xiao, N. J. Podraza, T. Filleter, C. Liu, Y. Yang, J. M. Luther, S. De Wolf, M. G. Kanatzidis, Y. Yan and E. H. Sargent, *Nature*, 2022, **613**, 676–681.
127 P. Xu, P. Wang, M. Wang, F. Sun, J. Leng, Y. Shi, S. Jin and W. Tian, *Nanomicro Lett.*, 2025, **17**, 285.
128 S. Tan, T. Huang, I. Yavuz, R. Wang, T. W. Yoon, M. Xu, Q. Xing, K. Park, D.-K. Lee, C.-H. Chen, R. Zheng, T. Yoon, Y. Zhao, H.-C. Wang, D. Meng, J. Xue, Y. J. Song, X. Pan, N.-G. Park, J.-W. Lee and Y. Yang, *Nature*, 2022, **605**, 268–273.
129 Q. Jiang, J. Tong, Y. Xian, R. A. Kerner, S. P. Dunfield, C. Xiao, R. A. Scheidt, D. Kuciauskas, X. Wang, M. P. Hautzinger, R. Tirawat, M. C. Beard, D. P. Fenning, J. J. Berry, B. W. Larson, Y. Yan and K. Zhu, *Nature*, 2022, **611**, 278–283.
130 Z. Li, B. Li, X. Wu, S. A. Sheppard, S. Zhang, D. Gao, N. J. Long and Z. Zhu, *Science*, 2022, **376**, 416–420.
131 J. Nie, Y. Zhang, J. Wang, L. Li and Y. Zhang, *ACS Energy Lett.*, 2024, **9**, 1674–1681.
132 P. Kumar, S. K. Sharma and R. Singh, *EES Sol.*, 2025, **1**, 356–365.
133 W. Q. Wu, Q. Wang, Y. Fang, Y. Shao, S. Tang, Y. Deng, H. Lu, Y. Liu, T. Li, Z. Yang, A. Gruverman and J. Huang, *Nat. Commun.*, 2018, **9**, 1625.
134 R. Berger, B. Grévin, P. Leclère and Y. Zhang, *Beilstein J. Nanotechnol.*, 2019, **10**, 132–134.
135 Z. Schumacher, A. Spielhofer, Y. Miyahara and P. Grutter, *Appl. Phys. Lett.*, 2017, **110**, 053111.
136 J. Murawski, T. Graupner, P. Milde, R. Raupach, U. Zerweck-Trogisch and L. M. Eng, *J. Appl. Phys.*, 2015, **118**, 154302.
137 R. Chen, C. Ni, J. Zhu, F. Fan and C. Li, *Nat. Protoc.*, 2024, **19**, 2250–2282.
138 Y. Almadori, D. Moerman, J. L. Martinez, P. Leclère and B. Grévin, *Beilstein J. Nanotechnol.*, 2018, **9**, 1695–1704.
139 B. Grévin, F. Husainy, D. Aldakov and C. Aumaître, *Beilstein J. Nanotechnol.*, 2023, **14**, 1068–1084.
140 E. J. Spadafora, R. Demadrille, B. Ratier and B. Grévin, *Nano Lett.*, 2010, **10**, 3337–3342.
141 P. A. Fernández Garrillo, Ł. Borowik, F. Caffy, R. Demadrille and B. Grévin, *ACS Appl. Mater. Interfaces*, 2016, **8**, 31460–31468.
142 L. Letertre, R. Roche, O. Douhéret, H. G. Kassa, D. Mariolle, N. Chevalier, Ł. Borowik, P. Dumas, B. Grévin, R. Lazzaroni and P. Leclère, *Beilstein J. Nanotechnol.*, 2018, **9**, 2087–2096.
143 T.-X. Qin, E.-M. You, M.-X. Zhang, P. Zheng, X.-F. Huang, S.-Y. Ding, B.-W. Mao and Z.-Q. Tian, *Light Sci. Appl.*, 2021, **10**, 84.
144 P. A. Fernández Garrillo, B. Grévin and Ł. Borowik, *Beilstein J. Nanotechnol.*, 2018, **9**, 1834–1843.
145 K. Atamanuk, J. Luria and B. D. Huey, *Beilstein J. Nanotechnol.*, 2018, **9**, 1802–1808.
146 R. Chen, Z. Ren, Y. Liang, G. Zhang, T. Dittrich, R. Liu, Y. Liu, Y. Zhao, S. Pang, H. An, C. Ni, P. Zhou, K. Han, F. Fan and C. Li, *Nature*, 2022, **610**, 296–301.
147 P. Qin, G. Yang, Z. Ren, S. H. Cheung, S. K. So, L. Chen, J. Hao, J. Hou and G. Li, *Adv. Mater.*, 2018, **30**, 1706126.
148 L. A. Pérez, N. Bajales and G. I. Lacconi, *Appl. Surf. Sci.*, 2019, **495**, 143539.
149 J. L. Pitters, I. A. Dogel and R. A. Wolkow, *ACS Nano*, 2011, **5**, 1984–1989.
150 M. Vrućinić, C. Matthiesen, A. Sadhanala, G. Divitini, S. Cacovich, S. E. Dutton, C. Ducati, M. Atatüre, H. Snaith, R. H. Friend, H. Sirringhaus and F. Deschler, *Adv. Sci.*, 2015, **2**, 1500136.
151 D. W. Pohl, U. Ch. Fischer and U. T. Dürig, *J. Microsc.*, 1988, **152**, 853–861.
152 D. W. Pohl, W. Denk and M. Lanz, *Appl. Phys. Lett.*, 1984, **44**, 651–653.
153 Y. De Wilde and P.-A. Lemoine, *AIP Conf. Proc.*, 2007, **931**, 43–52.
154 J. Nishida, A. H. Alfaifi, T. P. Gray, S. E. Shaheen and M. B. Raschke, *ACS Energy Lett.*, 2020, **5**, 1636–1643.
155 S. Schäffer, C. O. Ogolla, Y. Loth, T. Haeger, C. Kreusel, M. Runkel, T. Riedl, B. Butz, A. K. Wigger and P. H. Bolívar, *Nano Lett.*, 2023, **23**, 2074–2080.
156 Q. Xie, Y. Zhang, E. Janzen, J. H. Edgar and X. G. Xu, *Nat. Nanotechnol.*, 2024, **19**, 1108–1115.
157 F. Keilmann and R. Hillenbrand, *Philos. Trans. R. Soc., A*, 2004, **362**, 787–805.
158 Y. Yuan, J. Chae, Y. Shao, Q. Wang, Z. Xiao, A. Centrone and J. Huang, *Adv. Energy Mater.*, 2015, **5**, 1500615.
159 Y. Yoon, J. Chae, A. M. Katzenmeyer, H. P. Yoon, J. Schumacher, S. An, A. Centrone and N. Zhitenev, *Nanoscale*, 2017, **9**, 7771–7780.
160 Y. Zhang, Y. Wang, Z.-Q. Xu, J. Liu, J. Song, Y. Xue, Z. Wang, J. Zheng, L. Jiang, C. Zheng, F. Huang, B. Sun, Y.-B. Cheng and Q. Bao, *ACS Nano*, 2016, **10**, 7031–7038.
161 J. Chae, Q. Dong, J. Huang and A. Centrone, *Nano Lett.*, 2015, **15**, 8114–8121.
162 F. Mohn, L. Gross, N. Moll and G. Meyer, *Nat. Nanotechnol.*, 2012, **7**, 227–231.
163 L. Gross, F. Mohn, P. Liljeroth, J. Repp, F. J. Giessibl and G. Meyer, *Science*, 2009, **324**, 1428–1431.
164 W. Steurer, S. Fatayer, L. Gross and G. Meyer, *Nat. Commun.*, 2015, **6**, 8353.
165 W. Steurer, J. Repp, L. Gross, I. Scivetti, M. Persson and G. Meyer, *Phys. Rev. Lett.*, 2015, **114**, 036801.
166 S. Sahare, P. Ghoderao, S. B. Khan, Y. Chan and S.-L. Lee, *Nanoscale*, 2020, **12**, 15970–15992.
167 S. Gupta and S. Bhattacharyya, *Chem. Commun.*, 2024, **60**, 11685–11701.

Open Access Article. Published on 26 March 2026. Downloaded on 6/16/2026 7:27:17 AM. This article is licensed under a Creative Commons Attribution-NonCommercial 3.0 Unported Licence.

168 R. Ohmann, L. K. Ono, H.-S. Kim, H. Lin, M. V. Lee, Y. Li, N.-G. Park and Y. Qi, *J. Am. Chem. Soc.*, 2015, **137**, 16049–16054.
169 K. Leng, I. Abdelwahab, I. Verzhbitskiy, M. Telychko, L. Chu, W. Fu, X. Chi, N. Guo, Z. Chen, Z. Chen, C. Zhang, Q.-H. Xu, J. Lu, M. Chhowalla, G. Eda and K. P. Loh, *Nat. Mater.*, 2018, **17**, 908–914.
170 M. Telychko, S. Edalatmanesh, K. Leng, I. Abdelwahab, N. Guo, C. Zhang, J. I. Mendieta-Moreno, M. Nachtigall, J. Li, K. P. Loh, P. Jelínek and J. Lu, *Sci. Adv.*, 2022, **8**, eabj0395.
171 H.-C. Hsu, B.-C. Huang, S.-C. Chin, C.-R. Hsing, D.-L. Nguyen, M. Schnedler, R. Sankar, R. E. Dunin-Borkowski, C.-M. Wei, C.-W. Chen, P. Ebert and Y.-P. Chiu, *ACS Nano*, 2019, **13**, 4402–4409.
172 C. Stecker, K. Liu, J. Hieulle, R. Ohmann, Z. Liu, L. K. Ono, G. Wang and Y. Qi, *ACS Nano*, 2019, **13**, 12127–12136.
173 Y. Wang, B. Cui, Y. Zhao, T. Lin and J. Li, *Phys. Chem. Chem. Phys.*, 2024, **26**, 26192–26208.
174 M. Telychko and J. Lu, *Nano Mater. Sci.*, 2019, **1**, 260–267.
175 L. K. Ono and Y. Qi, *J. Phys. Chem. Lett.*, 2016, **7**, 4764–4794.
176 C. Ding, W. Dong, X. Jiao, Z. Zhang, G. Gong, Z. Wei, L. Wang, J.-F. Jia and Q.-K. Xue, *ACS Nano*, 2024, **18**, 17786–17793.
177 D. Halwidl, B. Stöger, W. Mayr-Schmölzer, J. Pavelec, D. Fobes, J. Peng, Z. Mao, G. S. Parkinson, M. Schmid, F. Mittendorfer, J. Redinger and U. Diebold, *Nat. Mater.*, 2016, **15**, 450–455.
178 J. Il Jake Choi, L. K. Ono, H. Cho, K.-J. Kim, H.-B. Kang, Y. Qi and J. Y. Park, *ACS Nano*, 2023, **17**, 25679–25688.
179 C. Mo, M. Yang, F. Sun, J. Jian, L. Zhong, Z. Fang, J. Feng and D. Yu, *Adv. Sci.*, 2020, **7**, 1902988.
180 S. Li, R. Ma, S. Xu, T. Zheng, G. Fu, Y. Wu, Z. Liao, Y. Kuang, Y. Hou, D. Wang, P. S. Petkov, K. Simeonova, X. Feng, L.-Z. Wu, X.-B. Li and T. Zhang, *J. Am. Chem. Soc.*, 2022, **144**, 13953–13960.
181 G. Fu, D. Yang, S. Xu, S. Li, Y. Zhao, H. Yang, D. Wu, P. S. Petkov, Z.-A. Lan, X. Wang and T. Zhang, *J. Am. Chem. Soc.*, 2024, **146**, 1318–1325.
182 J. Cheng, Y. Wu, W. Zhang, J. Zhang, L. Wang, M. Zhou, F. Fan, X. Wu and H. Xu, *Adv. Mater.*, 2024, **36**, 2305313.
183 J. Yang, A. Acharjya, M. Ye, J. Rabeah, S. Li, Z. Kochovski, S. Youk, J. Roeser, J. Grüneberg, C. Penschke, M. Schwarze, T. Wang, Y. Lu, R. van de Krol, M. Oschatz, R. Schomäcker, P. Saalfrank and A. Thomas, *Angew. Chem., Int. Ed.*, 2021, **60**, 19797–19803.
184 Y. Zhong, W. Dong, S. Ren and L. Li, *Adv. Mater.*, 2024, **36**, 2308251.
185 T. Sun, S. Li, L. Zhang and Y. Xu, *Angew. Chem., Int. Ed.*, 2023, **62**, e202306617.
186 X. Wu, W. Peng, Y. Yang, M. Lyu and J. Zhu, *ACS Appl. Mater. Interfaces*, 2026, **18**, 14361–14371.
187 W. Wu, H. Gao, L. Jia, Y. Li, D. Zhang, H. Zhan, J. Xu, B. Li, Z. Geng, Y. Cheng, H. Tong, Y. Pan, J. Liu, Y. He, X. Xu, Z. Li, B. He, M. Zhou, L. Wang and C. Qin, *Science*, 2025, **389**, 195–199.
188 P. Pansa-Ngat, S. Kamnoedmanee, N. Semapet, K. Sinthiptharakoon, C. Suwanchawalit, S. Burimart, C. Seriwattanachai, K. K. Shin Thant and P. Kanjanaboos, *ACS Appl. Energy Mater.*, 2024, **7**, 3234–3244.
189 B. S. Rodrigues, L. Polimante, C. A. Biffe, C. A. R. Costa and A. S. Polo, *ACS Omega*, 2026, **11**, 8061–8073.
190 J.-J. Li, J.-Y. Ma, Q.-Q. Ge, J.-S. Hu, D. Wang and L.-J. Wan, *ACS Appl. Mater. Interfaces*, 2015, **7**, 28518–28523.
191 Y. Shao, Y. Fang, T. Li, Q. Wang, Q. Dong, Y. Deng, Y. Yuan, H. Wei, M. Wang, A. Gruverman, J. Shield and J. Huang, *Energy Environ. Sci.*, 2016, **9**, 1752–1759.
192 Y. Adachi, H. F. Wen, Q. Zhang, M. Miyazaki, Y. Sugawara, H. Sang, J. Brndiar, L. Kantorovich, I. Štich and Y. J. Li, *ACS Nano*, 2019, **13**, 6917–6924.
193 Q. Zhang, Y. J. Li, H. F. Wen, Y. Adachi, M. Miyazaki, Y. Sugawara, R. Xu, Z. H. Cheng, J. Brndiar, L. Kantorovich and I. Štich, *J. Am. Chem. Soc.*, 2018, **140**, 15668–15674.
194 Z. Qu, Y. Sugawara and Y. Li, *J. Phys.: Condens. Matter*, 2023, **35**, 185001.
195 Z. Qu, J. Wei, Y. Sugawara and Y. Li, *Surf. Interfaces*, 2024, **49**, 104441.
196 Z. Qu, J. Wei, X. Liu, Y. Sugawara and Y. Li, *Surf. Sci.*, 2022, **724**, 1–7.
197 J. Xu and D. Chen, *J. Appl. Phys.*, 2021, **129**, 034301.
198 J. Song, Y. Zhou, N. P. Padture and B. D. Huey, *Nat. Commun.*, 2020, **11**, 3308.
199 A. Axt, I. M. Hermes, V. W. Bergmann, N. Tausendpfund and S. A. L. Weber, *Beilstein J. Nanotechnol.*, 2018, **9**, 1809–1819.
200 A. Guerrero, E. J. Juarez-Perez, J. Bisquert, I. Mora-Sero and G. Garcia-Belmonte, *Appl. Phys. Lett.*, 2014, **105**, 133902.
201 T. I. Kamins, *J. Appl. Phys.*, 1971, **42**, 4357–4365.
202 J. Y. W. Seto, *J. Appl. Phys.*, 1975, **46**, 5247–5254.
203 S. T. Anindo, D. Täuber and C. David, *J. Phys. Chem. C*, 2025, **06**, 42.
204 P. A. Fernández Garrillo, Ł. Borowik, F. Caffy, R. Demadrille and B. Grévin, *ACS Appl. Mater. Interfaces*, 2016, **8**, 31460–31468.
205 S. Sadewasser, P. Jelinek, C. K. Fang, O. Custance, Y. Yamada, Y. Sugimoto, M. Abe and S. Morita, *Phys. Rev. Lett.*, 2009, **103**, 266103.
206 S. Kawai, T. Glatzel, H. J. Hug and E. Meyer, *Nanotechnology*, 2010, **21**, 245704.
207 G. Cohen, E. Halpern, S. U. Nanayakkara, J. M. Luther, C. Held, R. Bennewitz, A. Boag and Y. Rosenwaks, *Nanotechnology*, 2013, **24**, 295702.
208 Z. M. Ma, L. Kou, Y. Naitoh, Y. J. Li and Y. Sugawara, *Nanotechnology*, 2013, **24**, 225701.
209 L. Kou, Z. Ma, Y. J. Li, Y. Naitoh, M. Komiyama and Y. Sugawara, *Nanotechnology*, 2015, **26**, 195701.

 © 2026 The Author(s). Published by the Royal Society of Chemistry